



The strength of the Brazilian fracture test

Aditya Kumar^a, Yangyuanchen Liu^b, John E. Dolbow^b, Oscar Lopez-Pamies^{c,*}

^a School of Civil and Environmental Engineering, Georgia Institute of Technology, Atlanta, GA 30332, USA

^b Department of Mechanical Engineering, Duke University, Durham, NC 27708, USA

^c Department of Civil and Environmental Engineering, University of Illinois, Urbana-Champaign, IL 61801, USA

ARTICLE INFO

Keywords:

Fracture nucleation
Strength
Brittle materials
Phase-field regularization

ABSTRACT

Since its introduction in the 1940s until present times, the so-called Brazilian test has been embraced by practitioners worldwide as a method of choice to indirectly measure the tensile strength of concrete, rocks, and other materials with a large compressive strength relative to their tensile strength. This is because of the ease that the test affords in both the preparation of the specimen (a circular disk) and the application of the loads (two platens compressing the specimen between them). Yet, this practical advantage has to be tempered by the fact that the observations from a Brazilian test — being an indirect experiment in the sense that it involves *not* uniform uniaxial tension but non-uniform triaxial stress states throughout the specimen — have to be appropriately interpreted to be useful. The main objective of this paper is to carry out a complete quantitative analysis of where and when fracture nucleates and propagates in a Brazilian test and thereby establish how to appropriately interpret its results. We do so by deploying the phase-field fracture theory of Kumar et al. (2020), which has been recently established as a complete theory of fracture capable of accurately describing the nucleation and propagation of cracks in linear elastic brittle materials under arbitrary quasistatic loading conditions. The last section of this paper puts forth a new protocol to deduce the tensile strength of a material from a Brazilian test that improves on the current ISRM and ASTM standards.

1. Introduction

Motivated by a grand engineering project concerning the relocation of a church in Rio de Janeiro by use of a platform standing on concrete rollers (see, e.g., Fairbairn and Ulm, 2002), Lobo Carneiro (1943) introduced the so-called Brazilian test — also referred to as the diametral compression test — as a convenient indirect experiment to infer the tensile strength of concrete. The test consists in compressing between two stiff platens a disk of the material of interest until the disk fractures; see Fig. 1. In contrast to standard direct tests aimed at subjecting specimens to uniform uniaxial tension, the Brazilian test is particularly accessible both in terms of specimen preparation and application of the loading. This practical advantage has to be tempered by the fact that the observations from a Brazilian test — being an indirect experiment in the sense that it involves *not* uniform uniaxial tension but non-uniform triaxial stress states throughout the specimen — have to be appropriately interpreted to be useful. The main objective of this work is precisely to establish how to appropriately interpret the results from a Brazilian test.

Soon after its introduction, it was recognized that the Brazilian test could be utilized to probe the tensile strength not just of concrete but, more generally, of nominally linear elastic brittle materials with a compressive strength significantly larger than their tensile strength, such as rocks and ceramics. This resulted in a flurry of theoretical and experimental investigations of the Brazilian

* Corresponding author.

E-mail addresses: aditya.kumar@ce.gatech.edu (A. Kumar), yangyc.liu@duke.edu (Y. Liu), john.dolbow@duke.edu (J.E. Dolbow), pamies@illinois.edu (O. Lopez-Pamies).

<https://doi.org/10.1016/j.jmps.2023.105473>

Received 2 June 2023; Received in revised form 19 September 2023; Accepted 21 October 2023

Available online 28 October 2023

0022-5096/© 2023 Elsevier Ltd. All rights reserved.

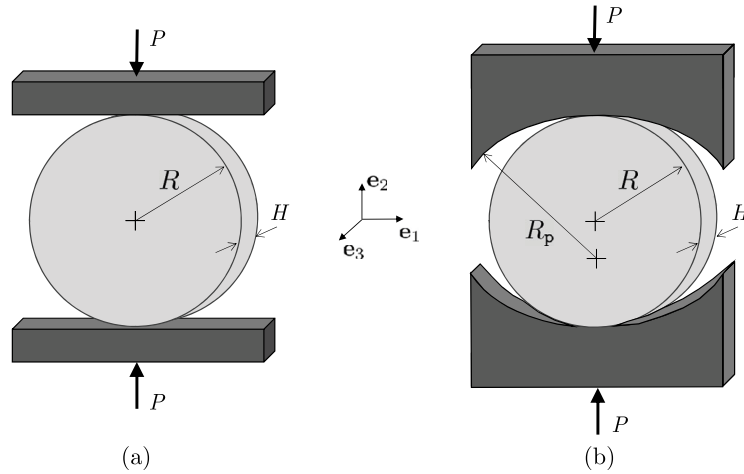


Fig. 1. Schematics of the Brazilian test for a specimen of radius R and thickness H under two standard types of loading configurations: (a) flat loading platens and (b) curved loading platens with radius of curvature R_p .

test for a wide range of materials, insomuch that the International Society for Rock Mechanics (ISRM) proposed a specific type of Brazilian test — one where curved platens of radius of curvature $R_p = 1.5R$, as opposed to flat ($R_p = +\infty$) platens, are used to apply the load to the specimens — as a standardized test to measure the tensile strength of rock materials (ISRM, 1978). The ISRM also suggested in their proposal the use of the formula

$$\sigma_{ts} = \frac{P_{max}}{\pi RH} \quad (1)$$

to deduce the tensile strength σ_{ts} from the test. In this expression, P_{max} stands for the maximum applied load indicated by the testing machine, while R is the radius of the disk and H is its thickness; see Fig. 1. As late as 2008, the American Society for Testing and Materials (ASTM) also advocated for the use of the formula (1) to deduce the tensile strength of rock materials from the Brazilian test, with the significant caveat that they considered (1) applicable to tests carried out with curved and flat platens alike (ASTM, 2008). The latest version of the ASTM standard (ASTM, 2016), however, considers the formula (1) only applicable for flat platens. When the test is carried out with curved ($R_p = 1.5R$) platens, the latest version of the ASTM standard suggests the use of the different formula

$$\sigma_{ts} = \frac{0.636P_{max}}{\pi RH}. \quad (2)$$

This long and yet ongoing history of the standardization of the Brazilian test hints both at its widespread popularity among practitioners and at the fact that the interpretation of its results to identify the tensile strength of materials remains unclear; for complementary accounts of the rich history of the Brazilian test, the interested reader is referred to the reviews by Andreev (1991), Erarslan and Williams (2012), Li and Wong (2013), and Garcia et al. (2017).

In this context, as alluded to above, the objective of this paper is to bring resolution to the interpretation of the experimental results from the Brazilian test by providing a complete quantitative description and explanation of where and when fracture nucleates and propagates in the specimens. The focus is on the prominent case of materials that can be considered homogeneous, isotropic, linear elastic brittle at the length scale of the specimens, this within the setting of quasistatic loading conditions. We do so by deploying the phase-field fracture theory recently initiated by Kumar et al. (2018a), in particular, we make use of its specialization to linear elastic brittle materials presented in Kumar et al. (2020).

In a nutshell, the theory initiated by Kumar et al. (2018a) corresponds to a generalization of the classical phase-field regularization (Bourdin et al., 2000) of the variational theory of brittle fracture of Francfort and Marigo (1998), which in turn corresponds to the mathematical statement of Griffith's fracture postulate in its general form of energy cost–benefit analysis (Griffith, 1921). Consistent with the vast experimental evidence that has been amassed for over a century on numerous ceramics, metals, and polymers alike, the generalization consists in accounting for the strength of the material at large, while keeping undisturbed the ability of the standard classical phase-field regularization to model crack propagation according to Griffith's fracture postulate. A string of recent works (Kumar et al., 2018b; Kumar and Lopez-Pamies, 2020; Kumar et al., 2020; Kumar and Lopez-Pamies, 2021; Kumar et al., 2022) have presented a wide range of validation results for a broad spectra of materials (silicone, titania, graphite, polyurethane, PMMA, alumina, natural rubber, glass), specimen geometries (with large and small pre-existing cracks, V notches, U notches, and smooth boundaries), and loading conditions furnishing encouraging evidence that the phase-field fracture theory initiated by Kumar et al. (2018a) may indeed provide a complete framework for the description of fracture nucleation and propagation in nominally elastic brittle materials under arbitrary quasistatic loads.

Before presenting and deploying in Sections 3 and 4 the phase-field fracture theory to describe and explain the Brazilian test, we begin in Section 2 by providing an elementary strength analysis of the problem. This analysis is aimed at clarifying a pervasive

misconception in the literature on the Brazilian test. To wit, the strength of an elastic brittle material is *not* just a point in stress space, but an entire surface¹

$$F(\boldsymbol{\sigma}) = 0, \quad (3)$$

where $\boldsymbol{\sigma}$ stands for the Cauchy stress tensor. Much like the Young's modulus E and Poisson's ratio ν , the strength surface (3) is an intrinsic (albeit stochastic) material property, one that is potentially very different for different materials. Now, it so happens that no material point in a Brazilian-test specimen ever experiences a state of uniaxial tension with $\boldsymbol{\sigma} = \text{diag}(\sigma > 0, 0, 0)$. As a result, the nucleation of a crack in a Brazilian-test specimen necessarily involves the satisfaction of the strength criticality condition (3) at a state of triaxial stress, or possibly at one of uniaxial compression, but *not* at one of uniaxial tension. In order to extrapolate that point in stress space to the tensile strength σ_{ts} of the material — that is, the point defined by the equation $F(\text{diag}(\sigma_{\text{ts}}, 0, 0)) = 0$ — requires having knowledge of more data points on the strength surface (3). An immediate implication of this basic observation is that, in principle, the formulas (1) and (2) are not expected to yield correct values for the tensile strength of the material.

Beyond making plain the critical importance of the high dimensionality of the strength surface (3), the results presented in Section 2 also serve to provide insight into the pivotal influence of the type of applied boundary conditions. The critical roles that the strength surface of the material and the type of applied boundary conditions play in the nucleation of fracture in a Brazilian test are investigated in full detail in Section 4, where we present representative results generated by the phase-field fracture theory laid out in Section 3. Section 4 also includes results that show the effect of the critical energy release rate G_c of the material on how cracks nucleate/propagate. We conclude this work by recording a summary of our findings and a number of final comments in Section 5. They include an assessment of the performance of the ISRM and ASTM formulas (1) and (2) and the proposal of a new protocol to deduce the tensile strength σ_{ts} of a material from a Brazilian test.

2. An elementary strength analysis of the Brazilian test

2.1. Initial configuration and kinematics

Consider a specimen in the form of a disk of radius $R = 25$ mm and thickness $H = 10$ mm in the \mathbf{e}_1 - \mathbf{e}_2 and \mathbf{e}_3 directions; see Fig. 1. These specific values for R and H are chosen here because they are representative of a typical specimen² and consistent with the ASTM recommendation that $0.4 \leq H/R \leq 1.5$ for a Brazilian-test specimen (ASTM, 2016). The Cartesian basis $\{\mathbf{e}_i\}$ stands for the laboratory frame of reference. Its origin is placed at the center of the specimen, so that, in its initial (undeformed and stress-free) configuration at time $t = 0$ the specimen occupies the domain

$$\Omega = \left\{ \mathbf{X} : \sqrt{X_1^2 + X_2^2} < R, |X_3| < \frac{H}{2} \right\}.$$

Making use of standard notation, we denote the boundary of the specimen by $\partial\Omega$ and its outward unit normal by \mathbf{N} . At a later time $t \in (0, T]$, in response to the applied boundary conditions described below in Section 2.3, the position vector \mathbf{X} of a material point in the specimen will move to a new position specified by

$$\mathbf{x} = \mathbf{X} + \mathbf{u}(\mathbf{X}, t), \quad (4)$$

where $\mathbf{u}(\mathbf{X}, t)$ is the displacement field. We write the associated strain at \mathbf{X} and t as

$$\mathbf{E}(\mathbf{u}) := \frac{1}{2} (\nabla \mathbf{u} + \nabla \mathbf{u}^T).$$

2.2. Constitutive behavior of the material: Elasticity, strength, and critical energy release rate

The specimen is taken to be made of a homogeneous, isotropic, linear elastic brittle material. Its mechanical behavior is hence characterized by three intrinsic properties: (i) its elasticity, (ii) its strength, and (iii) its critical energy release rate.

Elasticity. Precisely, granted isotropy, the elastic behavior of the material is characterized by the stored-energy function

$$W(\mathbf{E}(\mathbf{u})) = \mu \mathbf{E} \cdot \mathbf{E} + \frac{\lambda}{2} (\text{tr } \mathbf{E})^2, \quad (5)$$

where $\mu > 0$ and $\lambda > -2/3\mu$ are the Lamé constants, or, by the same token, by the stress–strain relation

$$\boldsymbol{\sigma}(\mathbf{X}, t) = \frac{\partial W}{\partial \mathbf{E}}(\mathbf{E}(\mathbf{u})) = 2\mu \mathbf{E} + \lambda (\text{tr } \mathbf{E}) \mathbf{I}.$$

¹ When a macroscopic piece of an elastic brittle material is subjected to a state of monotonically increasing *uniform* but otherwise arbitrary stress $\boldsymbol{\sigma}$, fracture will nucleate from one or more of its inherent defects at a critical value of that applied stress. The set of all such critical stresses defines the strength surface (3); see Section 2.1 in Kumar et al. (2020) and Lopez-Pamies (2023).

² In general, the thickness H of the specimen should be chosen to be at least 10 times larger than the characteristic length scale of the underlying microstructure, e.g., the size of the grains in a polycrystal, so that the specimen can be considered to be made of a homogeneous material.

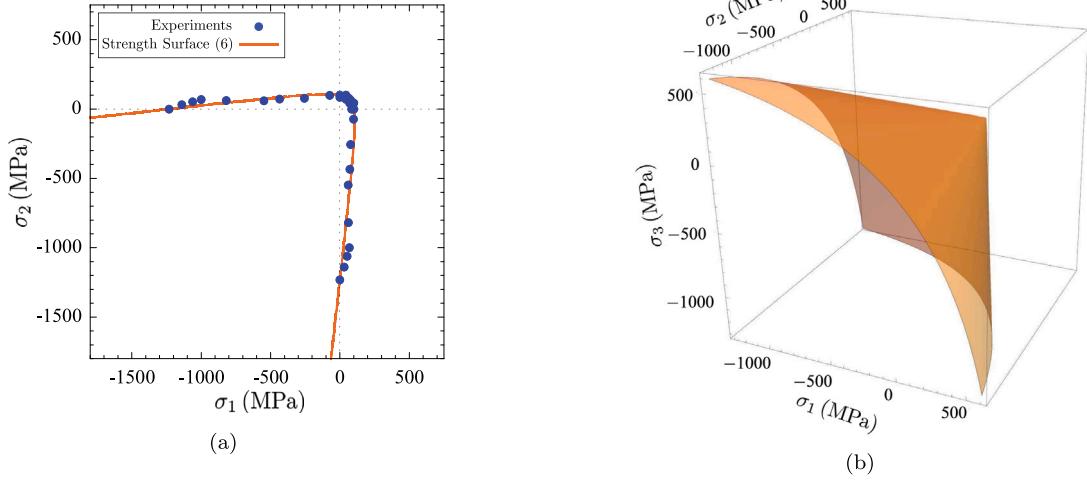


Fig. 2. (a) Comparison between the Drucker–Prager strength surface (6), with $\sigma_{ts} = 100$ MPa and $\sigma_{cs} = 1232$ MPa, and strength experimental data for titania (Ely, 1972); the results are plotted for the principal stress σ_2 in terms of the principal stress σ_1 and correspond to the case when $\sigma_3 = 0$. (b) Plot of the Drucker–Prager strength surface (6), with $\sigma_{ts} = 100$ MPa and $\sigma_{cs} = 1232$ MPa, in the space of all three principal stresses $(\sigma_1, \sigma_2, \sigma_3)$.

For the purposes of this section, recalling the basic relations $\mu = E/(2(1 + \nu))$ and $\lambda = E\nu/((1 + \nu)(1 - 2\nu))$, we will find it useful to rewrite the stress–strain relation in the alternative form

$$\sigma(\mathbf{X}, t) = \frac{E}{1 + \nu} \mathbf{E} + \frac{E\nu}{(1 + \nu)(1 - 2\nu)} (\text{tr } \mathbf{E}) \mathbf{I}$$

in terms of the Young’s modulus E and Poisson’s ratio ν .

Strength. For definiteness, the strength surface of the material is taken to be characterized by the Drucker–Prager strength surface

$$F(\sigma) = \sqrt{J_2} + \gamma_1 I_1 + \gamma_0 = 0 \quad \text{with} \quad \begin{cases} \gamma_0 = -\frac{2\sigma_{cs}\sigma_{ts}}{\sqrt{3}(\sigma_{cs} + \sigma_{ts})} \\ \gamma_1 = \frac{\sigma_{cs} - \sigma_{ts}}{\sqrt{3}(\sigma_{cs} + \sigma_{ts})} \end{cases}, \quad (6)$$

where

$$I_1 = \text{tr } \sigma \quad \text{and} \quad J_2 = \frac{1}{2} \text{tr } \sigma_D^2 \quad \text{with} \quad \sigma_D = \sigma - \frac{1}{3} (\text{tr } \sigma) \mathbf{I} \quad (7)$$

stand for two of the standard invariants of the stress tensor σ , while, again, the constants $\sigma_{ts} > 0$ and $\sigma_{cs} > 0$ denote the tensile and compressive strengths of the material, that is, they denote the critical stress values at which fracture nucleates under uniaxial tension $\sigma = \text{diag}(\sigma > 0, 0, 0)$ and uniaxial compression $\sigma = \text{diag}(\sigma < 0, 0, 0)$, respectively.

Remark 1. Note that, according to our choice of signs in (6), any stress state such that

$$F(\sigma) \geq 0$$

is in violation of the strength of the material.

Remark 2. The two-material-parameter strength surface (6), originally introduced by Drucker and Prager (1952) to model the yielding of soils, is arguably the simplest model that has proven capable of describing reasonably well the strength of many nominally brittle materials, thus its use here as a representative template. By way of an example, Fig. 2(a) shows the comparison between the strength surface (6), with $\sigma_{ts} = 100$ MPa and $\sigma_{cs} = 1232$ MPa, and the experimental data of Ely (1972) for titania. The results correspond roughly to the case when $\sigma_3 = 0$ and are plotted in the space of principal stresses (σ_1, σ_2) . For completeness, Fig. 2(b) shows the strength surface (6), with $\sigma_{ts} = 100$ MPa and $\sigma_{cs} = 1232$ MPa, in the space of all three principal stresses $(\sigma_1, \sigma_2, \sigma_3)$.

Critical energy release rate. Finally, the critical energy release rate (or intrinsic fracture energy) that describes the resistance to crack growth in the material is given by the non-negative constant

$$G_c.$$

Recall that, physically, the value of G_c denotes the total energy per unit fracture area expended in the creation of new surface originating from an existing crack within the material.

2.3. Boundary conditions: Evolving contact between the specimen and the platens

Consistent again with the ASTM recommendations, we consider that the specimen is placed between two curved platens whose separation (from pole to pole) is reduced from $D = 2R$ to $d < 2R$ at a constant rate. While the ASTM recommendation calls for curved platens of radius of curvature $R_p = +\infty$ or $R_p = 1.5R$, we shall consider curved platens of arbitrary radius of curvature $R_p > R$.

Accordingly, we have that the front and back boundaries

$$\partial\Omega_F = \left\{ \mathbf{X} : \sqrt{X_1^2 + X_2^2} < R, X_3 = \frac{H}{2} \right\} \quad \text{and} \quad \partial\Omega_B = \left\{ \mathbf{X} : \sqrt{X_1^2 + X_2^2} < R, X_3 = -\frac{H}{2} \right\}$$

of the specimen are always traction free, and so is the part $\partial\Omega_L \setminus \partial\Omega_L^{\text{contact}}$ of the lateral boundary

$$\partial\Omega_L = \left\{ \mathbf{X} : \sqrt{X_1^2 + X_2^2} = R, |X_3| < \frac{H}{2} \right\}$$

that is not in contact with the platens.

The part $\partial\Omega_L^{\text{contact}}$ of the lateral boundary $\partial\Omega_L$ that is in contact with the platens evolves as the change in separation $\Delta d = 2R - d$ between the platens increases. Assuming that the platens are rigid³ and that the friction at the specimen/platen interfaces is negligible,⁴ we have in particular that (see, e.g., Chapter 2 in the classical monograph by Kikuchi and Oden, 1988)

$$\begin{cases} g(\mathbf{u}(\mathbf{X}, t); \Delta d) \leq 0 \\ \sigma_N(\mathbf{X}, t) := \mathbf{N}(\mathbf{X}) \cdot \boldsymbol{\sigma}(\mathbf{X}, t)\mathbf{N}(\mathbf{X}) \leq 0 \\ \boldsymbol{\tau}(\mathbf{X}, t) := \boldsymbol{\sigma}(\mathbf{X}, t)\mathbf{N}(\mathbf{X}) - \sigma_N(\mathbf{X}, t)\mathbf{N}(\mathbf{X}) = \mathbf{0} \\ \sigma_N(\mathbf{X}, t) g(\mathbf{u}(\mathbf{X}, t); \Delta d) = 0 \end{cases}, \quad (\mathbf{X}, t) \in \partial\Omega_L \times [0, T], \quad (8)$$

where $g(\mathbf{u}(\mathbf{X}, t); \Delta d)$ is the so-called *gap function*. For the specific problem at hand here, as elaborated in Appendix A, it is given by the fully explicit expression

$$g(\mathbf{u}(\mathbf{X}, t); \Delta d) = \begin{cases} \sqrt{X_1^2 + (X_2 - R + R_p)^2} - R_p + \frac{X_1 u_1(\mathbf{X}, t) + (u_2(\mathbf{X}, t) + \frac{\Delta d}{2})(X_2 - R + R_p)}{\sqrt{X_1^2 + (X_2 - R + R_p)^2}}, & X_2 > 0 \\ \sqrt{X_1^2 + (X_2 + R - R_p)^2} - R_p + \frac{X_1 u_1(\mathbf{X}, t) + (u_2(\mathbf{X}, t) - \frac{\Delta d}{2})(X_2 + R - R_p)}{\sqrt{X_1^2 + (X_2 + R - R_p)^2}}, & X_2 < 0 \end{cases} \quad (9)$$

in terms of the in-plane components $u_1(\mathbf{X}, t)$ and $u_2(\mathbf{X}, t)$ of the displacement field and the applied separation Δd between the platens.

Remark 3. In the limit as $R_p \nearrow +\infty$, when the platens are flat, the gap function (9) simplifies to

$$g(\mathbf{u}(\mathbf{X}, t); \Delta d) = \begin{cases} X_2 - R + \frac{\Delta d}{2} + u_2(\mathbf{X}, t), & X_2 > 0 \\ -X_2 - R + \frac{\Delta d}{2} - u_2(\mathbf{X}, t), & X_2 < 0 \end{cases}.$$

Remark 4. By definition, the part of the lateral boundary $\partial\Omega_L$ that is in contact with the platens is simply given by

$$\partial\Omega_L^{\text{contact}} = \{ \mathbf{X} : g(\mathbf{u}(\mathbf{X}, t); \Delta d) = 0 \}.$$

Remark 5. Physically, condition (8)₁ is nothing more than a statement of the interpenetrability between the specimen and the platens. Conditions (8)_{2,3} — which define the normal and tangential components of the traction $\boldsymbol{\sigma}(\mathbf{X}, t)\mathbf{N}(\mathbf{X})$ on $\partial\Omega_L$ — describe the fact that the traction applied by the platens to the specimen must be normal to the specimen, consistent with the absence of friction, and compressive. Finally, condition (8)₄ determines that $\sigma_N(\mathbf{X}, t)$ may only be nonzero when the gap function $g(\mathbf{u}(\mathbf{X}, t); \Delta d) = 0$, that is, when the platen is in contact with the specimen at \mathbf{X} .

³ Typical platens are made of steel, which is significantly stiffer ($E_p \approx 200$ GPa) than many materials for which the Brazilian test is used. When testing very stiff materials (e.g., marble or alumina), however, the deformation of the platens must be taken into account. In this work, for clarity of presentation, we mostly restrict attention to the case when the platens can be considered as rigid.

⁴ Friction is expected to be negligible in the Brazilian test, primarily because the contact region between the specimen and the platens is small, more so the larger the radius of curvature R_p of the platens.

2.4. The governing equations of elastostatics

Prior to the nucleation of fracture, neglecting inertia and body forces, the combination of all the above ingredients with the balance of linear momentum leads to the following set of governing equations of elastostatics

$$\left\{ \begin{array}{l} \operatorname{div} \left[\frac{1}{2(1+\nu)} (\nabla \mathbf{u} + \nabla \mathbf{u}^T) + \frac{\nu}{(1+\nu)(1-2\nu)} (\operatorname{div} \mathbf{u}) \mathbf{I} \right] = \mathbf{0}, \quad (\mathbf{X}, t) \in \Omega \times [0, T] \\ \left[\frac{1}{2(1+\nu)} (\nabla \mathbf{u} + \nabla \mathbf{u}^T) + \frac{\nu}{(1+\nu)(1-2\nu)} (\operatorname{div} \mathbf{u}) \mathbf{I} \right] \mathbf{N} = \mathbf{0}, \quad (\mathbf{X}, t) \in \partial\Omega_F \cup \partial\Omega_B \times [0, T] \\ \left\{ \begin{array}{l} g(\mathbf{u}; \Delta d) \leq 0 \\ \frac{\sigma_N}{E} = \mathbf{N} \cdot \left[\frac{1}{2(1+\nu)} (\nabla \mathbf{u} + \nabla \mathbf{u}^T) + \frac{\nu}{(1+\nu)(1-2\nu)} (\operatorname{div} \mathbf{u}) \mathbf{I} \right] \mathbf{N} \leq 0 \\ \sigma_N g(\mathbf{u}; \Delta d) = 0 \end{array} \right. , \quad (\mathbf{X}, t) \in \partial\Omega_C \times [0, T] \\ \left[\frac{1}{2(1+\nu)} (\nabla \mathbf{u} + \nabla \mathbf{u}^T) + \frac{\nu}{(1+\nu)(1-2\nu)} (\operatorname{div} \mathbf{u}) \mathbf{I} \right] \mathbf{N} - \frac{\sigma_N}{E} \mathbf{N} = \mathbf{0} \\ \mathbf{u}(\mathbf{X}, 0) = \mathbf{0}, \quad \mathbf{X} \in \Omega \end{array} \right. \quad (10)$$

for the displacement field $\mathbf{u}(\mathbf{X}, t)$, where $g(\mathbf{u}; \Delta d)$ stands for the gap function (9) and where the Young's modulus E of the material has been factored out for convenience.

2.4.1. The elastostatics equations regularized

In general, Eqs. (10) do not admit analytical solutions and hence must be solved numerically. One challenge in doing so is dealing with the inequalities (10)_{3,4}. Over the past few decades, several approaches have been developed to deal with this type of unilateral constraints; see, e.g., Oden et al. (1980), Laursen (2003), and Wriggers (2006). The simplest among them is the penalty method. The basic idea consists in regularizing the inequalities (10)_{3,4} and equality (10)₅ by means of a *single equality*, containing a small non-negative parameter (or penalty), say ξ , that reduces to the constraints (10)₃₋₅ in the limit when that small parameter $\xi \searrow 0$. The resulting regularized elastostatics equations read

$$\left\{ \begin{array}{l} \operatorname{div} \left[\frac{1}{2(1+\nu)} (\nabla \mathbf{u} + \nabla \mathbf{u}^T) + \frac{\nu}{(1+\nu)(1-2\nu)} (\operatorname{div} \mathbf{u}) \mathbf{I} \right] = \mathbf{0}, \quad (\mathbf{X}, t) \in \Omega \times [0, T] \\ \left[\frac{1}{2(1+\nu)} (\nabla \mathbf{u} + \nabla \mathbf{u}^T) + \frac{\nu}{(1+\nu)(1-2\nu)} (\operatorname{div} \mathbf{u}) \mathbf{I} \right] \mathbf{N} = \mathbf{0}, \quad (\mathbf{X}, t) \in \partial\Omega_F \cup \partial\Omega_B \times [0, T] \\ \left[\frac{1}{2(1+\nu)} (\nabla \mathbf{u} + \nabla \mathbf{u}^T) + \frac{\nu}{(1+\nu)(1-2\nu)} (\operatorname{div} \mathbf{u}) \mathbf{I} \right] \mathbf{N} = -\frac{1}{\xi R E} \langle g(\mathbf{u}; \Delta d) \rangle \mathbf{N}, \quad (\mathbf{X}, t) \in \partial\Omega_C \times [0, T] \\ \mathbf{u}(\mathbf{X}, 0) = \mathbf{0}, \quad \mathbf{X} \in \Omega \end{array} \right. \quad (11)$$

where the triangular brackets stand for the operator $\langle f \rangle = (f + |f|)/2$ and, again, $g(\mathbf{u}; \Delta d)$ stands for the gap function (9). As the regularization parameter $\xi \searrow 0$, it can be shown that the solution of (11), say $\mathbf{u}^\xi(\mathbf{X}, t)$, converges to the solution $\mathbf{u}(\mathbf{X}, t)$ of (10).

From a physical point of view, it is useful to remark that the quantity ξ^{-1} represents the stiffness of the platens. From a practical point of view, the advantage of dealing with the regularized Eqs. (11), instead of dealing with (10) directly, is that they are nothing more than a standard — albeit nonlinear because of the nonlinear term $\langle g(\mathbf{u}; \Delta d) \rangle$ — boundary-value problem in elastostatics and hence are amenable to standard methods of solution. However, the approach suffers from ill-conditioning because of the smallness of the penalty parameter ξ . A robust way to circumvent this numerical difficulty is to use an augmented Lagrangian technique; see, e.g., Section 3.3.3 in the monograph by Laursen (2003). All the results presented below are generated with the standard finite-element (FE) method in conjunction with such a technique, the essential details of which are spelled out in Appendix B.

Remark 6. From a practical point of view, it is worth remarking here that the FE solutions of (11) have shown that the region of contact $\partial\Omega_C^{\text{contact}}$ and the component $u_2(\mathbf{X}, t)$ of the displacement field $\mathbf{u}(\mathbf{X}, t)$ at $\mathbf{X} \in \partial\Omega_C^{\text{contact}}$ are well approximated by the (asymptotic) Hertzian results

$$\partial\Omega_C^{\text{contact}} = \left\{ \mathbf{X} : \sqrt{X_1^2 + X_2^2} = R, |X_1| \leq \sqrt{\frac{R_p R \Delta d}{4(R_p - R)}}, |X_3| < \frac{H}{2} \right\}$$

and

$$u_2(\mathbf{X}, t) = \begin{cases} -\frac{\Delta d}{2} + \frac{(R_p - R)X_1^2}{2R_p R}, & X_2 > 0 \\ \frac{\Delta d}{2} - \frac{(R_p - R)X_1^2}{2R_p R}, & X_2 < 0 \end{cases} \quad (12)$$

Accordingly, for computational efficiency, one may make use of the asymptotic Hertzian boundary condition, wherein the displacement component (12) is directly prescribed, instead of the full contact boundary condition (10)₃ in generating solutions of (10).

2.5. Where and when the strength surface is violated

Having formulated the elastostatics problem (11), we are now in a position to investigate the pointwise stress field in the specimen during its loading in a Brazilian test, this prior to the nucleation of fracture. Because of the lack of geometric and loading singularities in the problem, remark that the resulting stress field is warranted to be bounded everywhere. This implies that the nucleation of fracture is expected to be dominated by the strength of the material; see Remark 7 below. The verity of this expectation is demonstrated below in Section 4.

In this section, in order to begin gaining quantitative insight into the first instance of fracture nucleation in a Brazilian test, we present results for where and when the strength surface of the material is violated in the specimen as the change in separation Δd between the platens increases, that is, for where and when

$$F(\boldsymbol{\sigma}) = \sqrt{J_2} + \frac{\sigma_{cs} - \sigma_{ts}}{\sqrt{3}(\sigma_{cs} + \sigma_{ts})} I_1 - \frac{2\sigma_{cs}\sigma_{ts}}{\sqrt{3}(\sigma_{cs} + \sigma_{ts})} \geq 0. \quad (13)$$

The results are based on FE solutions of (11) under the assumption of plane-stress conditions. Full three-dimensional simulations have confirmed that the specimen is indeed essentially under conditions of plane stress; to be precise, the full three-dimensional simulations show that the strength criterion (13) is always first reached on the front and back free boundaries before it is reached at the midplane of the specimens.

Aimed at separately identifying the effects of the properties of the material and of the geometry of the platens, the results pertain to three different compressive-to-tensile strength ratios, $\sigma_{cs}/\sigma_{ts} = 5, 8, 20$, three different Poisson's ratios, $\nu = 0.1, 0.3, 0.45$, and three different radii of curvature of the platens, $R_p = +\infty, 1.5R, 1.1R$. This particular set of representative values is selected here because it spans the entire range of possible scenarios.

Noting that the Young's modulus E does not enter the governing Eqs. (11) for the displacement field $\mathbf{u}(\mathbf{X}, t)$, all the results that follow are presented in terms of stresses that are normalized by E . For definiteness, we also set $\sigma_{ts} = 10^{-3}E$. That is, we make use of the normalization $\boldsymbol{\sigma} \mapsto E^{-1}\boldsymbol{\sigma}$, $\sigma_{ts} \mapsto \sigma_{ts}/E = 10^{-3}$, and $\sigma_{cs} \mapsto \sigma_{cs}/E$. The results are presented in terms of an also normalized global strain measure, namely, $\Delta d/(2R) = 1 - d/(2R) \in (0, 1]$.

Remark 7. Before proceeding with the presentation of the results, it is important to emphasize that satisfaction of the strength condition (13) at a material point \mathbf{X} is a necessary but *not* sufficient condition for fracture nucleation to occur at that point. This is because the stress field in a Brazilian-test specimen is highly non-uniform and hence the nucleation of fracture in such a test is governed neither solely by strength nor solely by the Griffith competition between the elastic and fracture energies, but by an “interpolation” between the two; see Section 2.3 in Kumar et al. (2020) and Lopez-Pamies (2023). Nevertheless, because the non-uniformity of the stress field is not exceedingly large (in particular, the stress is not singular), the expectation is that the nucleation of fracture is dominated by the strength of the material. The results in Section 4 will show that this is indeed the case.

2.5.1. The effect of the compressive-to-tensile strength ratio σ_{cs}/σ_{ts}

Fig. 3 presents contour plots of the regions (shown in black) of the specimen at which the criterion (13) is satisfied, and hence at which the strength of the material is exceeded, at four increasing values $\Delta d/(2R)$ of the global strain between the platens, that is, as the separation d between the platens is decreased and the specimen is compressed. The results are shown over the undeformed configuration and pertain to curved platens with radius of curvature $R_p = 1.5R$ and a material with Poisson's ratio $\nu = 0.3$ for three different values of its compressive-to-tensile strength ratio, $\sigma_{cs}/\sigma_{ts} = 5, 8, 20$.

There are several telltale observations from these results. First, irrespective of the value of the compressive-to-tensile strength ratio σ_{cs}/σ_{ts} , the region where the strength of the material is initially violated is always around the symmetry axes of the applied load. For the two smallest values $\sigma_{cs}/\sigma_{ts} = 5$ and $\sigma_{cs}/\sigma_{ts} = 8$, that region is equiaxed in shape and located near the platens, more so for the smallest value $\sigma_{cs}/\sigma_{ts} = 5$. For the largest value $\sigma_{cs}/\sigma_{ts} = 20$, on the other hand, the region where the strength of the material is initially violated is elongated in shape and is located around the center of the specimen.

Critically, for $\sigma_{cs}/\sigma_{ts} = 5$ and $\sigma_{cs}/\sigma_{ts} = 8$, when the strength is initially exceeded near the platens, the state of stress is approximately of the uniaxial compression form $(\sigma_1, \sigma_2, \sigma_3) \approx (0, -\sigma_\beta, 0)$ with $\sigma_\beta > 0$. By contrast, for $\sigma_{cs}/\sigma_{ts} = 20$, when the strength is initially exceeded around the center of the specimen, the state of stress is approximately of the triaxial form $(\sigma_1, \sigma_2, \sigma_3) \approx (\sigma_\alpha, -3\sigma_\alpha, 0)$ with $\sigma_\alpha > 0$; the precise maximum values of the ratio σ_1/σ_2 of principal stresses within the regions where the strength is initially violated is directly indicated in the plots for each of the three cases. Thus, as anticipated in the Introduction, the stress fields within all the regions that violate the strength of the material in the results shown in Fig. 3 are far from a state of uniaxial tension $(\sigma_1, \sigma_2, \sigma_3) = (\sigma > 0, 0, 0)$.

The above observations suggest that fracture nucleation, if it is dominated by the strength of the material as expected, is likely to occur around the center of the specimen for materials with large compressive-to-tensile strength ratios σ_{cs}/σ_{ts} . In the case that σ_{cs}/σ_{ts} is not sufficiently large, on the other hand, they suggest that fracture nucleation is likely to occur near the region of contact with the platens. This conclusion — which was already noticed in the early studies of the Brazilian test (Fairhurst, 1964; Colback, 1966) — is consistent with experimental observations.

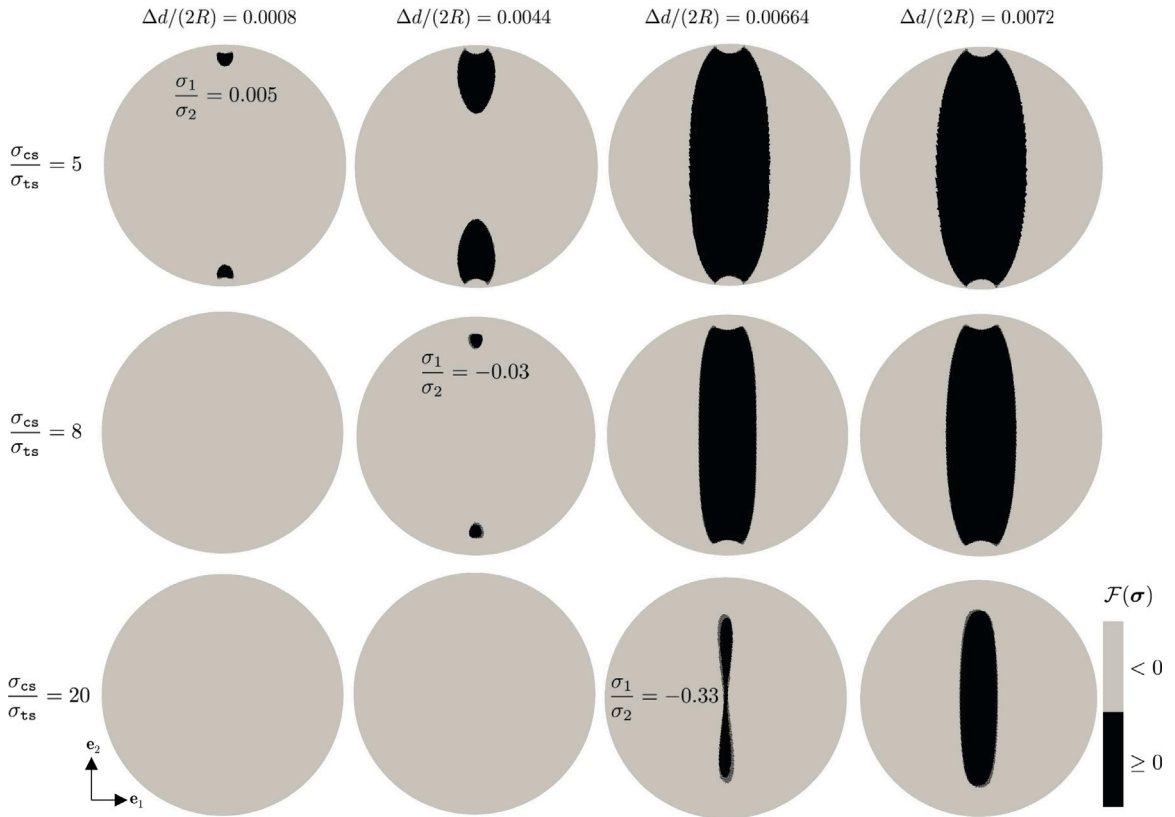


Fig. 3. Contour plots, over the undeformed configuration, of the regions of the specimen where the stress field exceeds $(F(\sigma) \geq 0)$ the Drucker–Prager strength surface of the material at four increasing values of the global strain $\Delta d/(2R)$ between the platens. The results correspond to curved platens with radius of curvature $R_p = 1.5R$ and a material with Poisson’s ratio $\nu = 0.3$ and three different values of the compressive-to-tensile strength ratio $\sigma_{cs}/\sigma_{ts} = 5, 8, 20$.

2.5.2. The effect of the Poisson’s ratio ν

From the setup of the Brazilian test, and even more so from the governing Eqs. (11) themselves, it is clear that the Poisson’s ratio ν of the material may have an impact on the resulting stress field in the specimen. Not surprisingly, akin to the compressive-to-tensile strength ratio σ_{cs}/σ_{ts} , the Poisson’s ratio ν was already recognized as a material property of interest in the early studies (Hondros, 1959).

To gain quantitative insight into the effect of ν on the nucleation of fracture in the Brazilian test, Fig. 4 presents contour plots of the regions of the specimen at which the strength criterion (13) is satisfied at four increasing values $\Delta d/(2R)$ of the global strain between the platens for a material with compressive-to-tensile strength ratio $\sigma_{cs}/\sigma_{ts} = 8$ and three different values of the Poisson’s ratio $\nu = 0.1, 0.3, 0.45$; note that these values correspond to bulk-to-shear-moduli ratios $\kappa/\mu \approx 1, 2, 10$, respectively. Much like in Fig. 3, the results are shown over the undeformed configuration and pertain to curved platens with radius of curvature $R_p = 1.5R$.

A quick glance suffices to realize that the results in Fig. 4 are qualitatively very similar to those in Fig. 3. The difference generated by different Poisson’s ratios ν is primarily quantitative in nature, but this quantitative difference is admittedly small. Consistent with basic intuition, it is such that the larger the Poisson’s ratio ν of the material, the smaller the global strain $\Delta d/(2R)$ that is needed to violate its strength surface.

2.5.3. The effect of the radius of curvature R_p of the platens

It is also apparent from the setup of the Brazilian test that the radius of curvature R_p of the platens (or, more generally, the specifics of how the forces are applied to the specimen through the contact with the platens) should have a significant impact on the resulting stress field in the specimen, especially near the poles. Early analytical and experimental studies confirmed as much; see, e.g., Colback (1966) and Awaji and Sato (1979).

To gain quantitative insight into the effect of R_p on the nucleation of fracture in the Brazilian test, Fig. 5 presents contour plots of the regions of the specimen at which the strength criterion (13) is satisfied at four increasing values $\Delta d/(2R)$ of the global strain between the platens for three different values of their radius of curvature $R_p = +\infty, 1.5R, 1.1R$; recall that $R_p = +\infty$ and $R_p = 1.5R$ are the two choices recommended by the ASTM standard. Much like in Figs. 3 and 4, the results are shown over the undeformed configuration and pertain to a material with Poisson’s ratio $\nu = 0.3$ and compressive-to-tensile strength ratio $\sigma_{cs}/\sigma_{ts} = 8$.

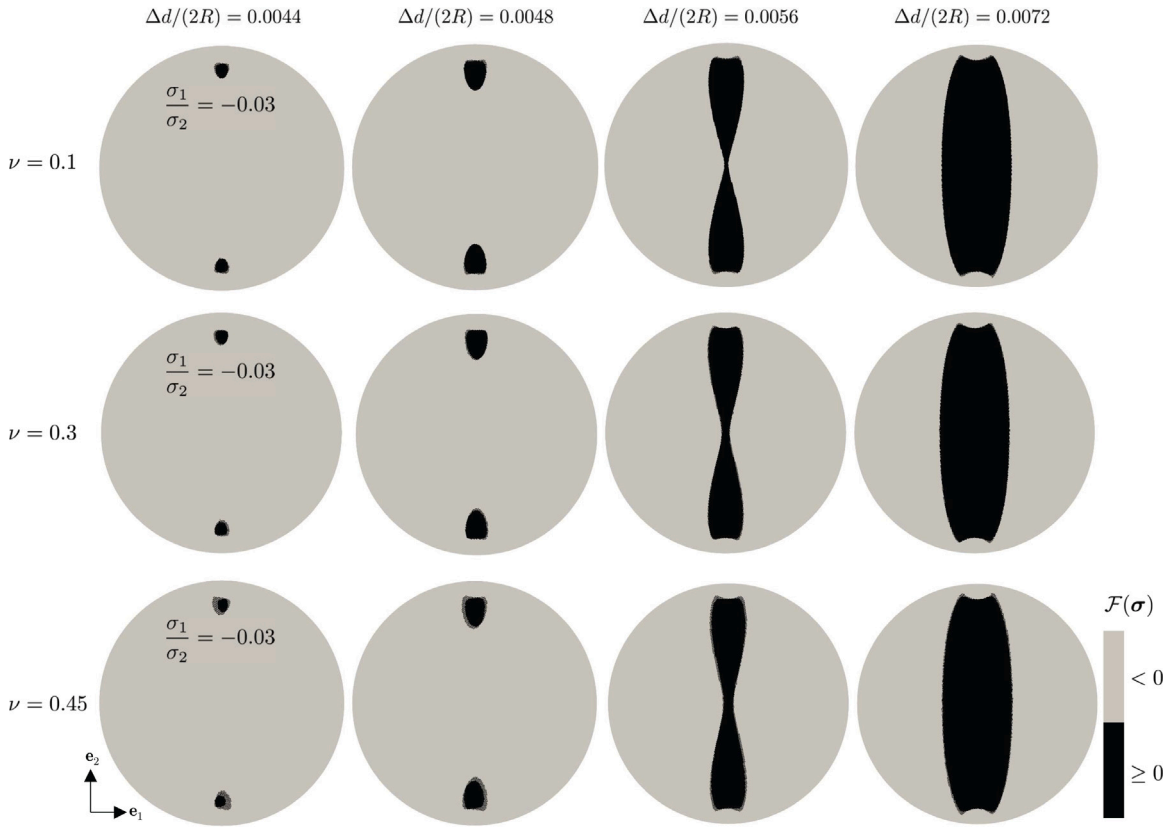


Fig. 4. Contour plots, over the undeformed configuration, of the regions of the specimen where the stress field exceeds ($F(\sigma) \geq 0$) the Drucker–Prager strength surface of the material at four increasing values of the global strain $\Delta d/(2R)$ between the platens. The results correspond to curved platens with radius of curvature $R_p = 1.5R$ and a material with compressive-to-tensile strength ratio $\sigma_{cs}/\sigma_{ts} = 8$ and three different values of Poisson’s ratio $\nu = 0.1, 0.3, 0.45$.

The main observation from the results presented in Fig. 5 is that the decrease of the radius of curvature R_p of the platens has a similar effect as the increase of the compressive-to-tensile strength ratio σ_{cs}/σ_{ts} of the material, namely, smaller values of R_p lead to the violation of the strength surface of the material to concentrate around the center of the specimen rather than near the platens.

In summary, the above elementary strength analysis suggests that the nucleation of fracture in a Brazilian test — if, again, it is indeed dominated by the strength of the material as expected — can occur either around the center of the specimen or near the region of contact with the platens. Specifically, nucleation of fracture around the center is more likely to occur in materials with a larger compressive-to-tensile strength ratio and for platens with a smaller radius of curvature R_p . On the other hand, nucleation near the region of contact with the platens is more likely to occur in materials with smaller compressive-to-tensile strength ratios and for platens with larger radius of curvature R_p . What is more, the analysis has made it plain that, irrespective of its location, nucleation of fracture will always occur in a region where the strength of the material is violated in a state of stress that is far from uniaxial tension.

Now, as emphasized in Remark 7, the violation (13) of the strength surface of the material, which is the focus of the above analysis, is a necessary but *not* sufficient condition for the nucleation of fracture. To determine where and when fracture actually nucleates and propagates in a Brazilian test one needs to make use of a complete theory of fracture. We do just that in the sequel.

3. A complete fracture nucleation and propagation analysis of the Brazilian test

In addition to the deformation (4), the boundary conditions (11)_{2,3} applied in a Brazilian test eventually result in the nucleation and subsequent propagation of cracks in the specimen. In the sequel, we describe such cracks in a regularized fashion via an order parameter or phase field

$$v = v(\mathbf{X}, t)$$

taking values in the range $[0, 1]$. The value $v = 1$ identifies the intact regions of the material and $v = 0$ those that have been fractured, while the transition from $v = 1$ to $v = 0$ is set to occur smoothly over regions of small thickness of regularization length scale $\epsilon > 0$.

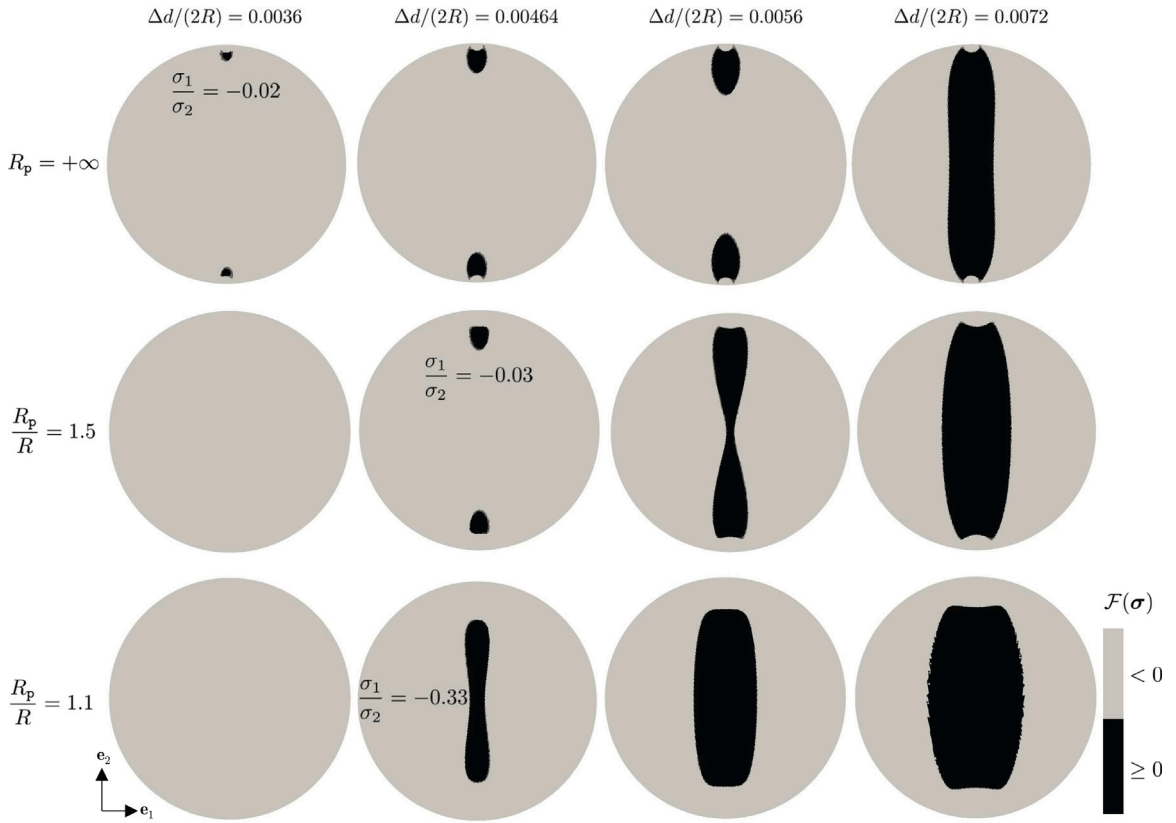


Fig. 5. Contour plots, over the undeformed configuration, of the regions of the specimen where the stress field exceeds ($F(\sigma) \geq 0$) the Drucker–Prager strength surface of the material at four increasing values of the global strain $\Delta d/(2R)$ between the platens. The results correspond to a material with Poisson’s ratio $\nu = 0.3$, compressive-to-tensile strength ratio $\sigma_{cs}/\sigma_{ts} = 8$, and platens of three different radii of curvature $R_p = +\infty, 1.5R, 1.1R$.

3.1. The governing equations of deformation and fracture

According to the specialization to the Brazilian test of interest in this work of the phase-field fracture theory put forth by Kumar et al. (2020) for linear elastic brittle materials, the displacement field $\mathbf{u}_k(\mathbf{X}) = \mathbf{u}(\mathbf{X}, t_k)$ and phase field $v_k(\mathbf{X}) = v(\mathbf{X}, t_k)$ at any material point $\mathbf{X} \in \bar{\Omega} = \Omega \cup \partial\Omega$ and at any given discrete time $t_k \in \{0 = t_0, t_1, \dots, t_m, t_{m+1}, \dots, t_M = T\}$ are determined by the system of coupled partial differential equations (PDEs)

$$\left\{ \begin{array}{l} \operatorname{div} \left[v_k^2 \frac{\partial W}{\partial \mathbf{E}}(\mathbf{E}(\mathbf{u}_k)) \right] = \mathbf{0}, \quad \mathbf{X} \in \Omega \\ \left[v_k^2 \frac{\partial W}{\partial \mathbf{E}}(\mathbf{E}(\mathbf{u}_k)) \right] \mathbf{N} = \mathbf{0}, \quad \mathbf{X} \in \partial\Omega_F \cup \partial\Omega_B \\ \left\{ \begin{array}{l} g(\mathbf{u}_k; \Delta d) \leq 0 \\ \sigma_{Nk} = \mathbf{N} \cdot \left[v_k^2 \frac{\partial W}{\partial \mathbf{E}}(\mathbf{E}(\mathbf{u}_k)) \right] \mathbf{N} \leq 0 \\ \sigma_{Nk} g(\mathbf{u}_k; \Delta d) = 0 \\ \left[v_k^2 \frac{\partial W}{\partial \mathbf{E}}(\mathbf{E}(\mathbf{u}_k)) \right] \mathbf{N} - \frac{\sigma_N}{E} \mathbf{N} = \mathbf{0} \end{array} \right. , \quad \mathbf{X} \in \partial\Omega_C \end{array} \right. \quad (14)$$

and

$$\left\{ \begin{array}{l} \operatorname{div} [\varepsilon G_c \nabla v_k] = \frac{8}{3} v_k W(\mathbf{E}(\mathbf{u}_k)) - \frac{4}{3} c_e(\mathbf{X}, t_k) - \frac{G_c}{2\varepsilon}, \quad \text{if } v_k(\mathbf{X}) < v_{k-1}(\mathbf{X}), \quad \mathbf{X} \in \Omega \\ \operatorname{div} [\varepsilon G_c \nabla v_k] \geq \frac{8}{3} v_k W(\mathbf{E}(\mathbf{u}_k)) - \frac{4}{3} c_e(\mathbf{X}, t_k) - \frac{G_c}{2\varepsilon}, \quad \text{if } v_k(\mathbf{X}) = 1 \text{ or } v_k(\mathbf{X}) = v_{k-1}(\mathbf{X}) > 0, \quad \mathbf{X} \in \Omega \\ v_k(\mathbf{X}) = 0, \quad \text{if } v_{k-1}(\mathbf{X}) = 0, \quad \mathbf{X} \in \Omega \\ \nabla v_k \cdot \mathbf{N} = 0, \quad \mathbf{X} \in \partial\Omega \end{array} \right. \quad (15)$$

with $\mathbf{u}(\mathbf{X}, 0) \equiv \mathbf{0}$ and $v(\mathbf{X}, 0) \equiv 1$. In these equations, we recall that the stored-energy function $W(\mathbf{E})$ is given by (5), $g(\mathbf{u}; \Delta d)$ denotes the gap function (9), $\nabla v_k = \nabla v(\mathbf{X}, t_k)$, and $c_e(\mathbf{X}, t)$ is a driving force whose specific constitutive prescription depends on the particular form of strength surface (3) of the material.

As in the preceding section, we assume that the strength surface of the material is characterized by the Drucker–Prager strength surface (6). For such a choice, making use of the constitutive prescription provided in Kumar et al. (2022), the driving force in (15) reads

$$c_e(\mathbf{X}, t) = \beta_2^\varepsilon \sqrt{J_2} + \beta_1^\varepsilon I_1 + \beta_0^\varepsilon + \frac{1}{v^3} \left(1 - \frac{\sqrt{I_1^2}}{I_1} \right) \left(\frac{J_2}{2\mu} + \frac{I_1^2}{6(3\lambda + 2\mu)} \right). \quad (16)$$

In this expression,

$$\begin{cases} \beta_0^\varepsilon = \delta^\varepsilon \frac{3G_c}{8\varepsilon} \\ \beta_1^\varepsilon = - \left(\frac{(1 + \delta^\varepsilon)(\sigma_{cs} - \sigma_{ts})}{2\sigma_{cs}\sigma_{ts}} \right) \frac{3G_c}{8\varepsilon} + \frac{\sigma_{ts}}{6(3\lambda + 2\mu)} + \frac{\sigma_{ts}}{6\mu} \\ \beta_2^\varepsilon = - \left(\frac{\sqrt{3}(1 + \delta^\varepsilon)(\sigma_{cs} + \sigma_{ts})}{2\sigma_{cs}\sigma_{ts}} \right) \frac{3G_c}{8\varepsilon} + \frac{\sigma_{ts}}{2\sqrt{3}(3\lambda + 2\mu)} + \frac{\sigma_{ts}}{2\sqrt{3}\mu} \end{cases}.$$

I_1 and J_2 stand for the invariants (7) of the Cauchy stress

$$\boldsymbol{\sigma}(\mathbf{X}, t) = v^2 \frac{\partial W}{\partial \mathbf{E}}(\mathbf{E}(\mathbf{u})) = 2\mu v^2 \mathbf{E} + \lambda v^2 (\text{tr } \mathbf{E}) \mathbf{I}$$

and, hence, read as

$$I_1 = (3\lambda + 2\mu)v^2 \text{tr } \mathbf{E}(\mathbf{u}) \quad \text{and} \quad J_2 = 2\mu^2 v^4 \text{tr } \mathbf{E}_D^2(\mathbf{u}), \quad \mathbf{E}_D(\mathbf{u}) = \mathbf{E}(\mathbf{u}) - \frac{1}{3} (\text{tr } \mathbf{E}(\mathbf{u})) \mathbf{I},$$

in terms of the displacement field \mathbf{u} and phase field v , and δ^ε is a unitless ε -dependent coefficient whose calibration needs to be carried out numerically.

Specifically, as elaborated in Subsection 4.3.2 in Kumar et al. (2020), for a given set of material constants λ , μ , G_c , σ_{ts} , σ_{cs} , a given finite regularization length ε , and mesh size h , the value of δ^ε is determined by considering any boundary-value problem of choice for which the nucleation from a large pre-existing crack can be determined exactly — according to Griffith’s sharp theory of brittle fracture for linear elastic materials — and then by having the phase-field theory (14)–(15) with external driving force (16) match that exact solution thereby determining δ^ε .

Remark 8. Physically, the calibration of the parameter δ^ε is what allows the governing Eqs. (14)–(15) to spouse the concept of strength in the bulk with the concept of Griffith energy competition at crack singularities. As illustrated in Appendix C, this calibration is directly related to a family of material length scales that is intrinsic to the theory and that comes about because the evolution Eq. (15) for the phase field depends on material inputs of different units. Precisely, the elastic stored-energy function $W(\mathbf{E}(\mathbf{u}))$ and the strength surface $\mathcal{F}(\boldsymbol{\sigma}) = 0$ have units of *force/length*², while the critical energy release rate G_c has units of *force/length*. Their combination in Eq. (15) leads to the family of material length scales in the theory.

Remark 9. The inequalities in (15) stem from the facts that, by definition, the phase field is bounded according to $0 \leq v \leq 1$ and, by constitutive assumption, fracture is an irreversible process, in other words, healing is not allowed. Incidentally, recent experimental evidence has revealed that internally nucleated cracks in elastomers may self-heal (Poulain et al., 2017, 2018). The inequalities (15) can be augmented to describe such a healing process; see Subsection 3.2 in Kumar et al. (2018a) for the relevant details and Francfort et al. (2019) for the corresponding “sharp-theory” perspective.

Remark 10. The regularization length ε in (15) is a parameter that is void of any physical meaning. In practice, it should be selected to be significantly smaller than the smallest characteristic length scale in the structural problem at hand, as well as no significantly larger than the smallest material length scale built in (14)–(15); see Appendix C. Provided that ε is selected in this manner, the predictions generated by the governing Eqs. (14)–(15) are essentially independent of ε ; see, e.g., Subsection 4.3 in Kumar et al. (2020) and the Appendix in Kumar et al. (2022). In this work, it suffices to consider regularization lengths that are smaller than the thickness of the specimen. All the results that are presented below correspond to $\varepsilon \leq H/10 = 1$ mm.

3.2. The governing equations regularized

In general, Eqs. (14)–(15) can only be solved numerically. To do so, in addition to dealing with the contact inequalities (14)_{3,4} for the displacement field \mathbf{u} already discussed above, we also have to deal with the inequalities in (15), which, as noted in Remark 9, enforce that the phase field remains in the physically admissible range $0 \leq v \leq 1$ and that fracture is irreversible. Following the

Table 1Values of the regularization length ϵ , FE mesh size h , and the parameter δ^ϵ utilized in the simulations.

σ_{cs}/σ_{ts}	G_c (N/m)	ϵ (mm)	Mesh size h (mm)	δ^ϵ
5	100	0.7	0.05	6
5	500	3.5	0.1	11
5	1000	0.5	0.05	2.65
8	1000	1.2	0.1	4
20	1000	5	0.2	23

same strategy as in Section 2.4.1, here too we opt to make use of the penalty method to regularize these inequalities. Precisely, we consider the regularized set of governing equations

$$\begin{cases} \operatorname{div} \left[v_k^2 \frac{\partial W}{\partial \mathbf{E}}(\mathbf{E}(\mathbf{u}_k)) \right] = \mathbf{0}, & \mathbf{X} \in \Omega \\ \left[v_k^2 \frac{\partial W}{\partial \mathbf{E}}(\mathbf{E}(\mathbf{u}_k)) \right] \mathbf{N} = \mathbf{0}, & \mathbf{X} \in \partial\Omega_F \cup \partial\Omega_B \\ \left[v_k^2 \frac{\partial W}{\partial \mathbf{E}}(\mathbf{E}(\mathbf{u}_k)) \right] \mathbf{N} = -\frac{1}{\xi} \frac{1}{R \mu} \langle g(\mathbf{u}_k; \Delta d) \rangle \mathbf{N}, & \mathbf{X} \in \partial\Omega_C \end{cases} \quad (17)$$

and

$$\begin{cases} \operatorname{div} [\epsilon G_c \nabla v_k] = \frac{8}{3} v_k W(\mathbf{E}(\mathbf{u}_k)) - \frac{4}{3} c_e(\mathbf{X}, t_k) - \frac{G_c}{2\epsilon} + \frac{8}{3\zeta} p(v_{k-1}, v_k), & \mathbf{X} \in \Omega \\ \nabla v_k \cdot \mathbf{N} = 0, & \mathbf{X} \in \partial\Omega \end{cases} \quad (18)$$

with

$$p(v_{k-1}, v_k) = H(v_\alpha - v_k) (|v_{k-1} - v_k| - (v_{k-1} - v_k)) + |1 - v_k| - (1 - v_k) - |v_k| + v_k, \quad (19)$$

$\mathbf{u}(\mathbf{X}, 0) \equiv \mathbf{0}$, and $v(\mathbf{X}, 0) \equiv 1$ for the displacement field $\mathbf{u}_k(\mathbf{X}) = \mathbf{u}(\mathbf{X}, t_k)$ and the phase field $v_k(\mathbf{X}) = v(\mathbf{X}, t_k)$ at any material point $\mathbf{X} \in \bar{\Omega} = \Omega \cup \partial\Omega$ and at any given discrete time $t_k \in \{0 = t_0, t_1, \dots, t_m, t_{m+1}, \dots, t_M = T\}$.

Much like in simpler equations of elastostatics (11), the triangular brackets in Eq. (17)₃ stand for the operator $\langle f \rangle = (f + |f|)/2$, $g(\mathbf{u}; \Delta d)$ denotes the gap function (9), and the regularization parameter ξ should be selected to be small relative to the stiffness of the material. To circumvent the ill-conditioning caused by the smallness of ξ , we make use of the same augmented Lagrangian treatment spelled out in Appendix B to solve the elastostatics equations (11). For further computational efficiency, one may alternatively use a Hertzian boundary condition; see Remark 6 above.

In the regularization (or penalty) function (19) entering Eq. (18)₁, $H(\cdot)$ stands for the Heaviside function and $v_\alpha = 0.05$ denotes the value below which the phase field v is considered to be non-increasing in time; see Remark 4 in Kumar et al. (2020). Also, the regularization parameter ζ should be selected to be small relative to term $2\epsilon/G_c$. All the results that are presented below correspond to $\zeta^{-1} = 10^4 G_c / (2\epsilon)$.

On their own, the regularized Eqs. (17) and (18) are second-order PDEs for the displacement field \mathbf{u} and the phase field v . Accordingly, their numerical solution is amenable to a standard FE staggered scheme in which (17) and (18) are discretized with finite elements and solved iteratively one after the other at every time step t_k until convergence is reached. All the simulations presented below are generated with such a scheme, making use of unstructured meshes and plane-stress conditions, as implemented in a modification of the FEniCS code of the theory of Kumar et al. (2020) available in GitHub⁵ that accounts for the boundary condition (17)₃ of contact, as well as in a MOOSE implementation of the theory also available in GitHub.⁶

4. Results and discussion

Having spelled out the governing Eqs. (17)–(18), we are now in a position to investigate where and when cracks nucleate and propagate in a Brazilian test.

Throughout this section, we consider specimens with the same radius $R = 25$ mm and thickness $H = 10$ mm considered in the preceding section. For definiteness, we take the specimens to be made of a material with Young's modulus and Poisson's ratio

$$E = 100 \text{ GPa} \quad \text{and} \quad \nu = 0.20.$$

These values are representative of various common types of glasses, ceramics, and rocks. We also consider that the strength surface of the material is of the Drucker–Prager form (6) with uniaxial tensile and compressive strengths

$$\sigma_{ts} = 200, 125, 50 \text{ MPa} \quad \text{and} \quad \sigma_{cs} = 1000 \text{ MPa}.$$

⁵ https://github.com/adityakr42/FEniCS_Fracture_Kumar_Lopez-Pamies

⁶ <https://github.com/hugary1995/raccoon>

These correspond to the same ratios $\sigma_{cs}/\sigma_{ts} = 5, 8, 20$ considered in the preceding section and are also characteristic of various glasses, ceramics, and rocks. Finally, we consider the values

$$G_c = 100, 500, 1000 \text{ N/m.}$$

for the critical energy release rate of the material. Table 1 provides the values of the regularization length ϵ , the FE mesh size h , and the corresponding values of the parameter δ^ϵ for all the pairs σ_{cs}/σ_{ts} and G_c for which results are presented in the next three subsections. The values of the mesh size h in Table 1 were checked to be small enough to lead to spatially converged FE solutions.

4.1. The effect of the compressive-to-tensile strength ratio σ_{cs}/σ_{ts}

Fig. 6 presents results from simulations carried out on specimens with the three different compressive-to-tensile strength ratios $\sigma_{cs}/\sigma_{ts} = 5, 8, 20$. The results correspond to curved platens with radius of curvature $R_p = 1.5R$ and specimens with critical energy release rate $G_c = 1000 \text{ N/m}$. Part (a) of the figure plots the normalized force $P/(\pi RH)$ exerted by the platens as a function of the normalized applied displacement $\Delta d/(2R)$; note that the particular choice of normalization for the force is so that its value $P/(\pi RH)$ can be directly related to the ISRM and ASTM formulas (1) and (2). Part (b) of the figure presents the corresponding contour plots of the phase field v at three select values of the normalized force $P/(\pi RH)$. Specifically, the first column shows results at around the first instance when the phase field v decreases from its initial value of 1, which happens to coincide with the instance when the strength surface of the material $\mathcal{F}(\sigma) = 0$ is first violated. The second and third columns show results just before and just after v localizes near 0; recall that the localization of the phase field v near 0 corresponds to the nucleation or propagation of a crack. To aid the discussion, the regions of the specimen where the strength surface $\mathcal{F}(\sigma) = 0$ of the material is violated are delineated by a white line in the first two columns of the contour plots.

There are several key observations to be made from the results in Fig. 6. First, for all three compressive-to-tensile strength ratios σ_{cs}/σ_{ts} , Fig. 6(a) shows that the force $P/(\pi RH)$ increases monotonically with increasing normalized applied displacement $\Delta d/(2R)$ between the platens until reaching a local maximum beyond which it suddenly drops to a small value. The sudden drop occurs at larger values of the force $P/(\pi RH)$ for smaller ratios σ_{cs}/σ_{ts} , that is, for materials with larger uniaxial tensile strength σ_{ts} .

As shown by the third column of the contour plots in Fig. 6(b), the sudden drop in the force in Fig. 6(a) is the manifestation of the appearance of a crack splitting the specimen into disconnected pieces. The first and second columns of the contour plots in Fig. 6(b) reveal the formation process of that splitting crack. In general, the pattern of the splitting crack is not symmetric due, in part, to its brutal appearance and, in part, to the unstructured nature of the FE mesh. For these reasons, different meshes lead to similar, yet not identical, patterns.

For the specimens with the two smallest compressive-to-tensile strength ratios $\sigma_{cs}/\sigma_{ts} = 5$ and 8, the first column of contour plots shows that the phase field v first decreases from its initial value of 1 near the platens as a consequence of the strength surface $\mathcal{F}(\sigma) = 0$ of the material being violated there. Upon further loading, the second column of contour plots shows that the region where $v < 1$ grows in size, but still v does not quite localize near 0. This growth is also the direct result of the strength surface being violated. Note, in particular, that at this stage the strength of the material has been exceeded at the center of the specimen. Upon further loading the phase field v finally localizes near 0 and the splitting crack is formed. The appearance of the crack is brutal, making it difficult to separate its nucleation from its propagation.

For the specimen with the largest compressive-to-tensile strength $\sigma_{cs}/\sigma_{ts} = 20$, the formation process of the splitting crack is similar to that for $\sigma_{cs}/\sigma_{ts} = 5$ and 8, with the key difference that the initial decrease of the phase field v takes places around the center of the specimen, and not near the platens, since that is the location in the specimen where the strength of the material is initially exceeded.

The above description of the formation process of the splitting crack is consistent with direct visual observations reported in the literature for, e.g., granite aplite and dolerite (Colback, 1966), Carrara marble (Wong et al., 2014), and PMMA (Garcia-Fernandez et al., 2018).

Summing up, the results in Fig. 6 show that the process of nucleation of fracture in the Brazilian test is indeed dominated by the strength of the material, with the caveat that the first violation of the strength surface $\mathcal{F}(\sigma) = 0$ in the specimen does *not* correspond to the instance when the force exerted by the platens reaches the peak value that precedes the appearance of a splitting crack. Instead, the stress *around the center* of the specimen must be in violation of the strength of the material for the splitting crack to appear. The difference between the instance at which the strength of the material is first violated and that at which the splitting crack forms can be admittedly large. For instance, in terms of the value of the normalized force $P/(\pi RH)$, this difference is about 50% for the specimen with ratio $\sigma_{cs}/\sigma_{ts} = 5$. By contrast, the difference between the instance at which the strength of the material is first violated *around the center* of the specimen and that at which the splitting crack forms is small. In terms, again, of the value of the normalized force $P/(\pi RH)$, it is less than 1% for all three ratios $\sigma_{cs}/\sigma_{ts} = 5, 8$, and 20.

4.2. The effect of the radius of curvature R_p of the platens

Fig. 7 presents results analogous to those in Fig. 6 from simulations carried out with platens of the three different radii of curvature $R_p = +\infty, 1.5R, 1.1R$. The results correspond to specimens with compressive-to-tensile strength ratio $\sigma_{cs}/\sigma_{ts} = 8$ and critical energy release rate $G_c = 1000 \text{ N/m}$.

Similar to the conclusion established in Section 2 when comparing Figs. 5 to 3, the main observation from the results presented in Fig. 7 is that the decrease of the radius of curvature R_p of the platens has a similar effect as the increase of the compressive-to-tensile strength ratio σ_{cs}/σ_{ts} of the material.

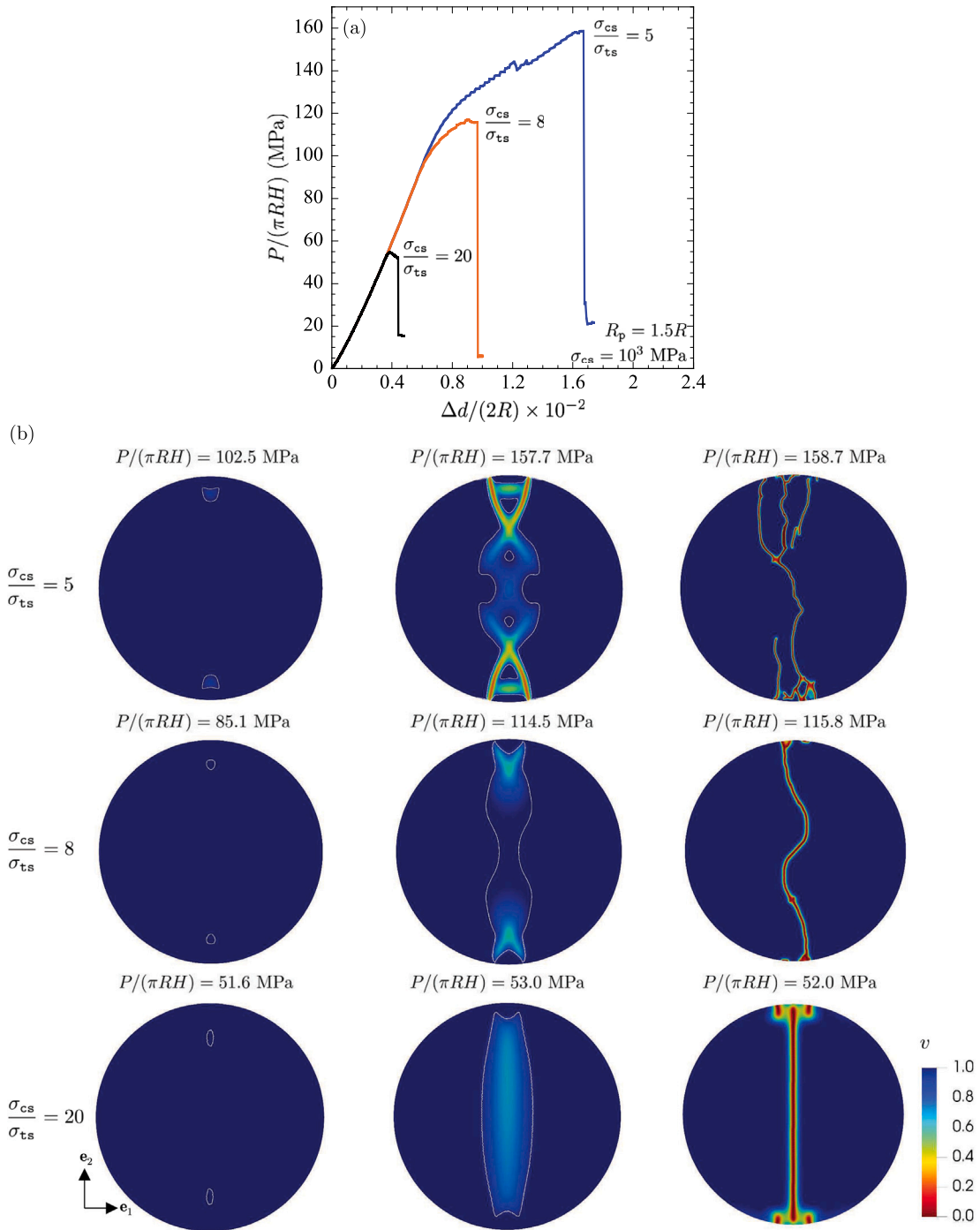


Fig. 6. Simulations of Brazilian tests carried out with curved platens of radius of curvature $R_p = 1.5R$ on specimens with three different compressive-to-tensile strength ratios $\sigma_{cs}/\sigma_{ts} = 5, 8, 20$ and critical energy release rate $G_c = 1000$ N/m. (a) The normalized force $P/(\pi RH)$ as a function of the normalized applied displacement $\Delta d/(2R)$. (b) Contour plots, over the undeformed configuration, of the phase field v at three select values of the normalized force $P/(\pi RH)$; the white line in first two columns delineates the regions of the specimen where the strength surface $F(\sigma) = 0$ of the material is violated.

In particular, smaller values of R_p lead to larger peak normalized forces $P/(\pi RH)$ preceding the appearance of a splitting crack. The location where the phase field v first decreases from 1 also depends on R_p in a similar manner as on σ_{cs}/σ_{ts} . Accordingly, for the two largest radii of curvature $R_p = +\infty$ and $1.5R$, the first column of the contour plots in Fig. 7(b) shows that $v < 1$ near the platens. For the smallest value $R_p = 1.1R$, the corresponding contour plot shows that $v < 1$ around the center of the specimen.

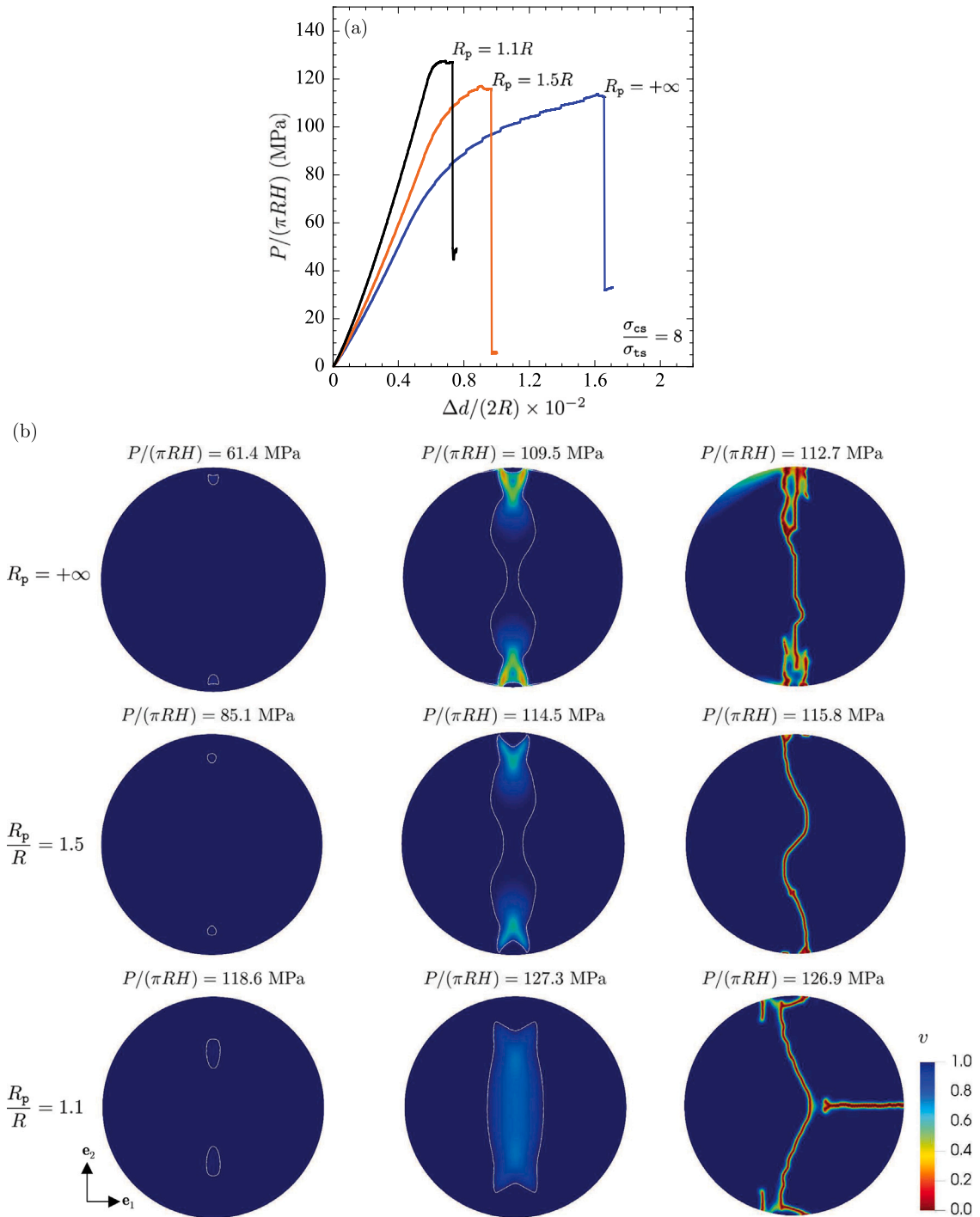


Fig. 7. Simulations of Brazilian tests on specimens with compressive-to-tensile strength ratio $\sigma_{cs}/\sigma_{ts} = 8$ and critical energy release rate $G_c = 1000$ N/m, carried out with platens of three different radii of curvature $R_p = +\infty, 1.5R, 1.1R$. (a) The normalized force $P/(\pi RH)$ as a function of the normalized applied displacement $\Delta d/(2R)$. (b) Contour plots, over the undeformed configuration, of the phase field v at three select values of the normalized force $P/(\pi RH)$.

Moreover, the difference between the instance at which the strength of the material is first violated (the first column in Fig. 7(b)) and that at which the splitting crack is formed (the third column in Fig. 7(b)) can be large, in excess of 85%. By contrast, the

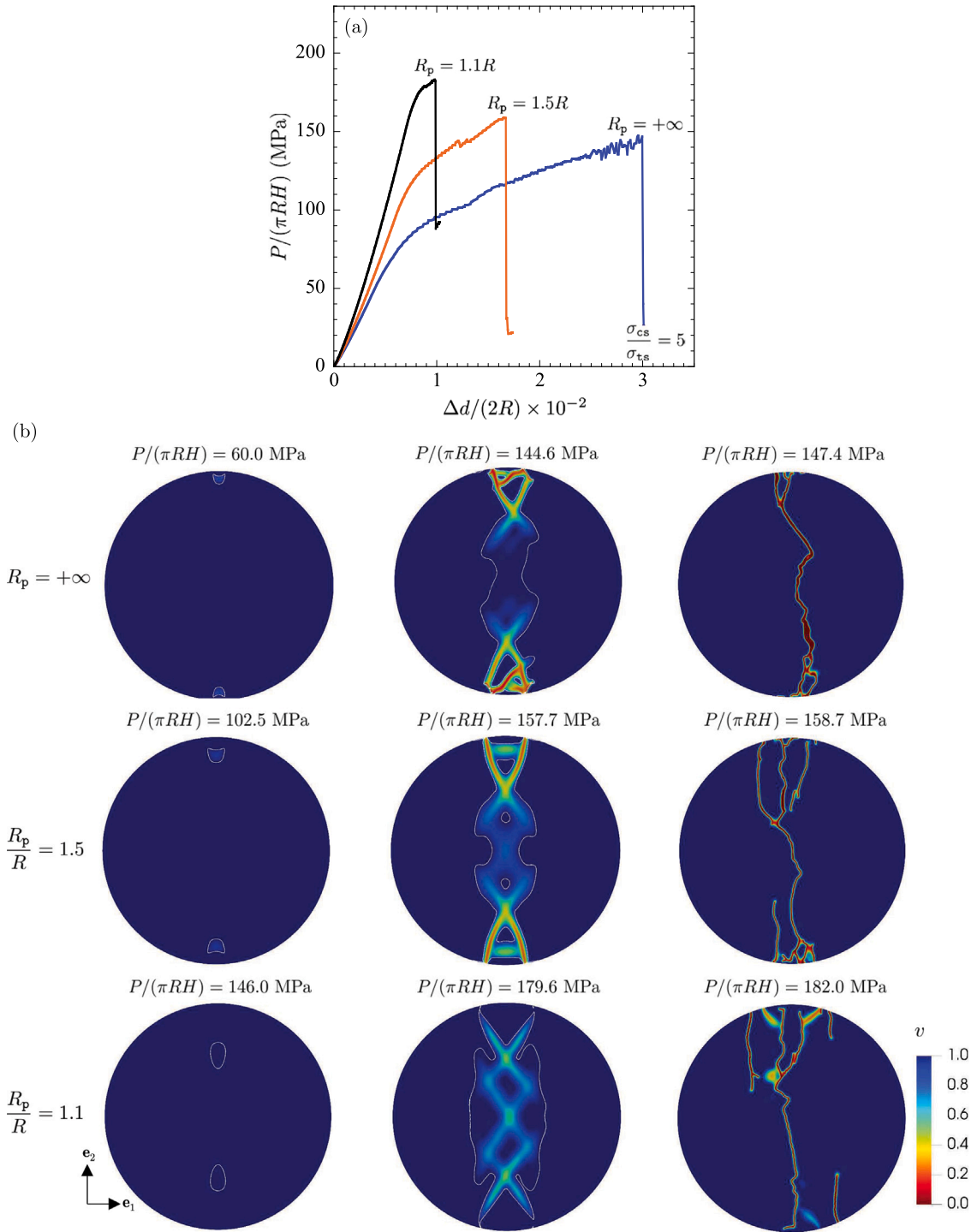


Fig. 8. Simulations of Brazilian tests on specimens with compressive-to-tensile strength ratio $\sigma_{cs}/\sigma_{ts} = 5$ and critical energy release rate $G_c = 1000$ N/m, carried out with platens of three different radii of curvature $R_p = +\infty, 1.5R, 1, 1R$. (a) The normalized force $P/(\pi RH)$ as a function of the normalized applied displacement $\Delta d/(2R)$. (b) Contour plots, over the undeformed configuration, of the phase field v at three select values of the normalized force $P/(\pi RH)$.

difference between the instance at which the strength of the material is first violated around the center of the specimen (the second column in Fig. 7(b)) and that at which the splitting crack is formed is relatively small. In terms of the value of the normalized force $P/(\pi RH)$, the difference is less than 3% for $R_p = +\infty$ and $1.5R$ and about 6% for $R_p = 1.1R$.

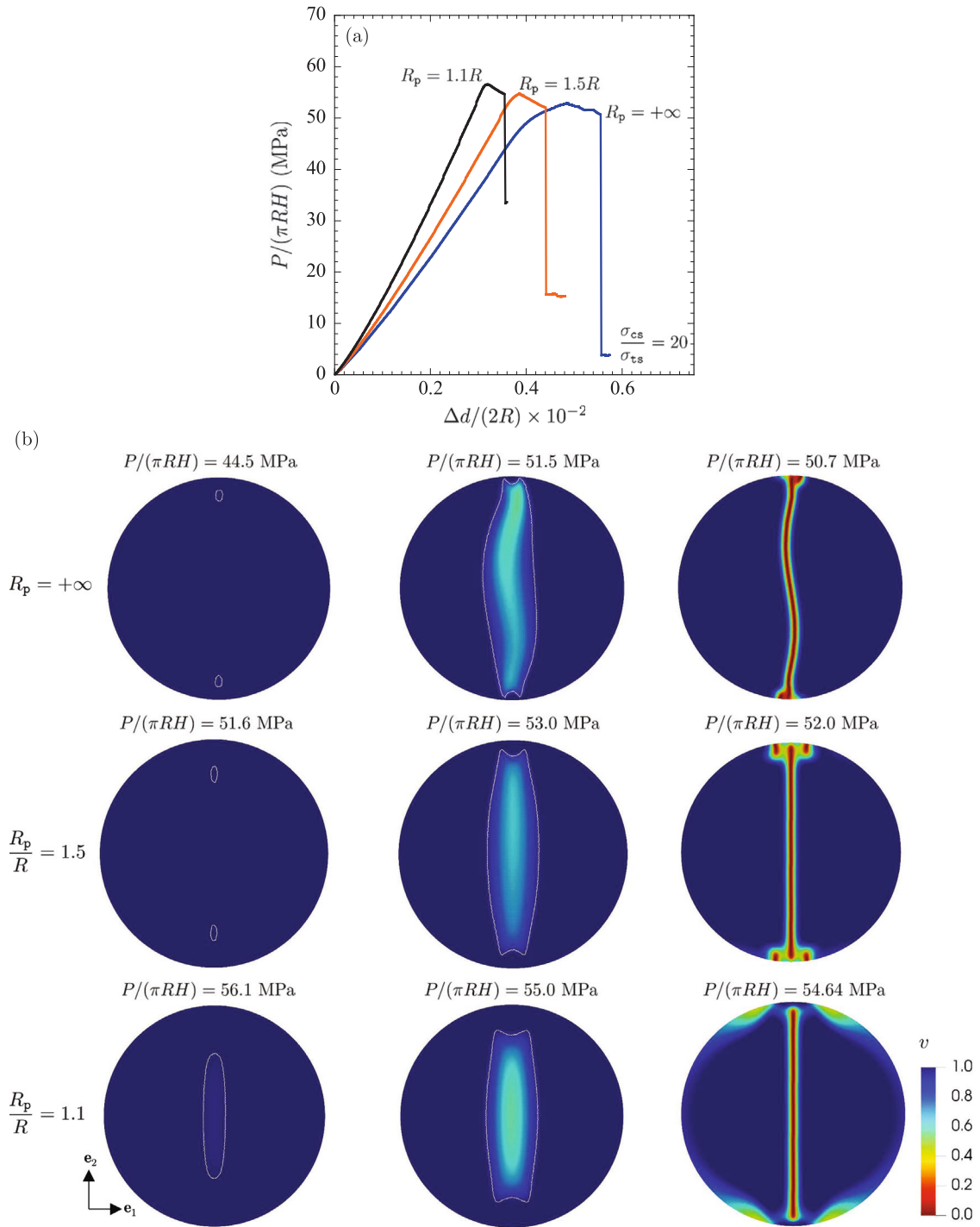


Fig. 9. Simulations of Brazilian tests on specimens with compressive-to-tensile strength ratio $\sigma_{cs}/\sigma_{ts} = 20$ and critical energy release rate $G_c = 1000$ N/m, carried out with platens of three different radii of curvature $R_p = +\infty, 1.5R, 1.1R$. (a) The normalized force $P/(\pi RH)$ as a function of the normalized applied displacement $\Delta d/(2R)$. (b) Contour plots, over the undeformed configuration, of the phase field v at three select values of the normalized force $P/(\pi RH)$.

For completeness, Figs. 8 and 9 present results analogous to those presented in Fig. 7 for specimens with compressive-to-tensile strength ratios $\sigma_{cs}/\sigma_{ts} = 5$ and 20. Of note from these results is the fact that, again, the value of the normalized force $P/(\pi RH)$ at which the strength of the material is first violated around the center of the specimens (the second columns in Figs. 8(b) and 9(b)) is similar to the value at which the splitting crack is formed (the third columns in Figs. 8(b) and 9(b)).

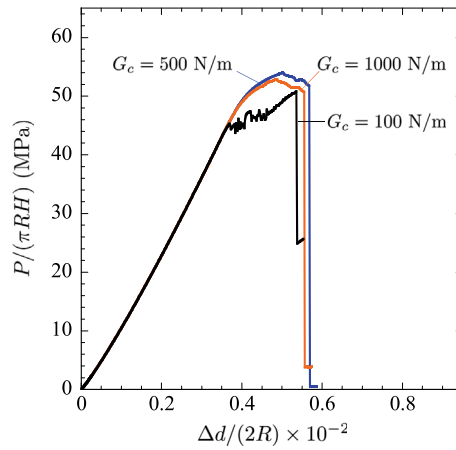


Fig. 10. The normalized force $P/(\pi RH)$ as a function of the normalized applied displacement $\Delta d/(2R)$ from simulations of Brazilian tests carried out with flat ($R_p = +\infty$) platens on specimens with compressive-to-tensile strength ratio $\sigma_{cs}/\sigma_{ts} = 20$ and three different critical energy release rates $G_c = 100, 500, 1000$ N/m.

4.3. The effect of the critical energy release rate G_c

All the results presented in Figs. 6 through 9 above pertain to specimens with the same value $G_c = 1000$ N/m of the critical energy release rate. In order to gain insight into the effect of G_c on how cracks nucleate/propagate in a Brazilian test, Fig. 10 presents results from simulations carried out on specimens with the three different values $G_c = 100, 500, 1000$ N/m. They correspond to flat ($R_p = +\infty$) platens, specimens with compressive-to-tensile strength ratio $\sigma_{cs}/\sigma_{ts} = 20$, and show the normalized force $P/(\pi RH)$ exerted by the platens as a function of the normalized applied displacement $\Delta d/(2R)$.

A quick glance at Fig. 10 suffices to realize that the three sets of force–deformation responses are very similar to one another and hence that the critical energy release rate G_c of the specimen does not have a very significant effect in the Brazilian test. These results serve to further confirm that the nucleation of fracture in a Brazilian test is dominated first and foremost by the strength of the material.

5. Summary and a new protocol to deduce σ_{ts} from a Brazilian test

The where. For materials that can be considered homogeneous, isotropic, linear elastic brittle, and that feature a compressive strength σ_{cs} that is larger by at least a factor of 5 than their tensile strength σ_{ts} , the analysis presented in this work has established that fracture in a Brazilian test will nucleate either around the center of the specimen or near the region of contact with the platens.

The use of flat ($R_p = +\infty$) platens favors the nucleation of fracture near the region of contact with the platens, while the use of curved platens with a radius of curvature R_p that is comparable to that of the specimen, e.g., $R_p = 1.1R$, favors the nucleation around the center of the specimen.

In addition to the platens' radius of curvature, the location where fracture nucleates is also strongly dependent on the compressive-to-tensile strength ratio σ_{cs}/σ_{ts} of the material. Materials with a compressive strength that is much larger than their tensile strength favor a nucleation of fracture around the center of the specimen. On the other hand, materials with a compressive strength that is larger but not much larger than their tensile strength favor a nucleation of fracture near the region of contact with the platens.

Irrespective of the location of its nucleation, the process of fracture in a Brazilian test invariably leads to the ultimate appearance of a crack in the direction of the applied load that splits the specimen into disconnected pieces. The appearance of this splitting crack is brutal, making it difficult to distinguish its nucleation from its propagation.

The when. The analysis presented in this work has established as well that fracture in a Brazilian test is dominated first and foremost by the strength of the material.

Precisely, irrespective of its location, the nucleation of fracture involves the violation of the strength surface $F(\sigma) = 0$ of the material at stress states that are in the mixed quadrant ($\sigma_1 \geq 0, \sigma_2 < 0, 0$) in the space of principal stresses ($\sigma_1, \sigma_2, 0$). The nucleation of fracture around the center of the specimen involves the violation of the strength surface around a stress state of the form $(\sigma_\alpha, -3\sigma_\alpha, 0)$ with $\sigma_\alpha > 0$ — that is, a stress state with strong stress triaxiality — while the nucleation of fracture near the region of contact with the platens involves the violation of the strength surface around the stress state $(0, -\sigma_\beta, 0)$ with $\sigma_\beta > 0$ — that is, a stress state of uniaxial compression.

Critically, by the time that a crack splitting the specimen into disconnected pieces appears, the strength surface $F(\sigma) = 0$ of the material has already been violated not just at a sole material point X but over a sizable subdomain of the specimen. In other words, the peak or maximum force P_{max} in the force–deformation response of the specimen that signals the appearance of a splitting crack in the Brazilian test does *not* correlate with the first instance at which the strength of the material is exceeded.

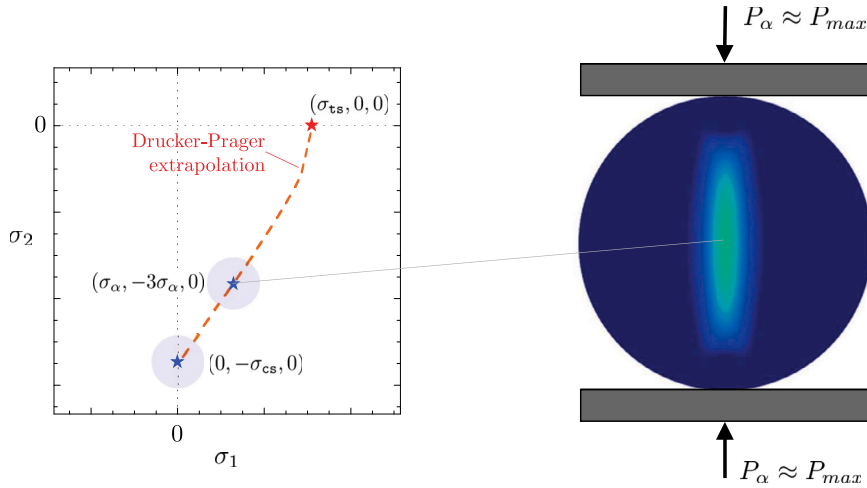


Fig. 11. Schematic illustrating that the formula (21) corresponds to the extrapolation of the strength point $F = (\text{diag}(\sigma_\alpha, -3\sigma_\alpha, 0)) = 0$, with $\sigma_\alpha = P_{max}/(\pi RH)$ obtained from a Brazilian test carried out with flat ($R_p = +\infty$) platens, and the point of uniaxial compressive strength $F = (\text{diag}(0, -\sigma_{cs}, 0)) = 0$ to the point of uniaxial tensile strength $F = (\text{diag}(\sigma_{ts}, 0, 0)) = 0$ in the space of principal stresses $(\sigma_1, \sigma_2, 0)$. The point $\sigma = \text{diag}(\sigma_\alpha, -3\sigma_\alpha, 0)$ corresponds to the violation of the strength surface of the material at the center of the specimen.

Nevertheless, the analysis has revealed that the value of the force, P_α say, at which the strength surface $F(\sigma) = 0$ is first violated around the center of specimen is relatively close to the value of the maximum force P_{max} at which a splitting crack appears. As elaborated next, this correlation can be exploited to establish a direct link between the maximum force P_{max} measured in a Brazilian test and the tensile strength σ_{ts} of the material being tested.

5.1. A new protocol to deduce the tensile strength σ_{ts} of a material from a Brazilian test

As emphasized from the outset, practitioners make use of the Brazilian test to estimate the tensile strength σ_{ts} of a material of interest. They do so by directly linking the maximum force P_{max} measured by the testing machine prior to the splitting of the specimen to σ_{ts} via one of the formulas (1) or (2).

Yet, as anticipated in the Introduction, and as demonstrated throughout this paper and summarized above, this protocol is incongruous on two counts. First, the nucleation of fracture in a Brazilian test involves the violation of the strength surface $F(\sigma) = 0$ of the material at points in stress space that are far from a state of uniaxial tension where $\sigma = \text{diag}(\sigma > 0, 0, 0)$. Second, by the time that the maximum force P_{max} leading to the splitting of the specimen is reached, the strength of the material has already been exceeded over large parts of the specimen.

Thus, the only rational way that the maximum force P_{max} measured from a Brazilian test can be used to estimate σ_{ts} is to first establish a link between P_{max} and a corresponding point on the strength surface $F(\sigma) = 0$ of the material and to then extrapolate that point to the point of uniaxial tensile strength $F(\text{diag}(\sigma_{ts}, 0, 0)) = 0$.

As remarked above, the results presented in Section 4 have shown that the force P_α at which the strength surface $F(\sigma) = 0$ of the material is first violated around the center of the specimen happens to be well approximated by the maximum force P_{max} , especially when the test is carried out with flat ($R_p = +\infty$) platens. Making use of the classical solution of Hondros (1959), recalled in Appendix D for completeness, this approximation allows us to directly link the force P_{max} with the point

$$(\sigma_1, \sigma_2, \sigma_3) = (\sigma_\alpha, -3\sigma_\alpha, 0) = \left(\frac{P_{max}}{\pi RH}, -\frac{3P_{max}}{\pi RH}, 0 \right) \tag{20}$$

on the strength surface $F(\sigma) = 0$ of the material.

Having determined the point (20) on the surface $F(\sigma) = 0$ directly in terms of the maximum force P_{max} measured from a Brazilian test carried out with flat ($R_p = +\infty$) platens, the final step is to extrapolate (20) to the point $F(\text{diag}(\sigma_{ts}, 0, 0)) = 0$ so as to estimate the uniaxial tensile strength σ_{ts} of the material. Here, as illustrated schematically by Fig. 11, we propose to do so by assuming that the strength surface $F(\sigma) = 0$ of the material can be described as a Drucker–Prager strength surface (6), which, as noted in Remark 2 above, has been shown to be descriptive of many nominally elastic brittle materials. Such a model is fully characterized by two points in stress space and hence provides a unique extrapolation to $F(\text{diag}(\sigma_{ts}, 0, 0)) = 0$ from knowledge of (20) and the uniaxial compressive strength σ_{cs} . A straightforward calculation shows that the extrapolated result for σ_{ts} is given by the formula

$$\sigma_{ts} = f(P_{max}, \sigma_{cs}) \frac{P_{max}}{\pi RH}, \tag{21}$$

Table 2
Accuracy of the values of the uniaxial tensile strength σ_{ts} predicted by the formula (21).

σ_{ts} (MPa)	σ_{cs}/σ_{ts}	P_{max} (kN)	$f(P_{max}, \sigma_{cs})$	Predicted σ_{ts} (MPa)	σ_{ts}^- (MPa)	σ_{ts}^+ (MPa)
200	5	116	1.363	201	119	201
125	8	89	1.174	132	90	154
50	20	41	0.942	50	42	72

where $f(P_{max}, \sigma_{cs})$ is a factor that, as indicated by its arguments, depends on the maximum force P_{max} measured in the test and the uniaxial compressive strength σ_{cs} of the material. It is given by the fully explicit expression

$$f(P_{max}, \sigma_{cs}) = \frac{(\sqrt{13} - 2) \frac{\pi RH}{P_{max}} \sigma_{cs}}{\frac{2\pi RH}{P_{max}} \sigma_{cs} - \sqrt{13} - 2}. \tag{22}$$

The following remarks are in order.

- Being based on the analysis presented in Section 4, aimed at understanding the Brazilian test for standard concrete, rocks, and ceramics, the formula (21) with (22) applies to materials with compressive-to-tensile strength ratios $\sigma_{cs}/\sigma_{ts} \geq 5$. Whether it remains applicable to materials with $\sigma_{cs}/\sigma_{ts} < 5$ would be worth studying in future work.
- Noting that the formula (21) with (22) can be rearranged in the form $P_{max}/(\pi RH) = 2\sigma_{ts}\sigma_{cs}/[(2 + \sqrt{13})\sigma_{ts} - (2 - \sqrt{13})\sigma_{cs}]$, we can readily deduce that the factor (22) can be rewritten solely in terms of the compressive-to-tensile strength ratio σ_{cs}/σ_{ts} as follows:

$$f = \frac{\sqrt{13}}{2} - 1 + \left(\frac{\sqrt{13}}{2} + 1 \right) \frac{\sigma_{ts}}{\sigma_{cs}}.$$

This result makes it apparent that the factor (22) is a monotonically decreasing function of the compressive-to-tensile strength ratio σ_{cs}/σ_{ts} , one that is bounded from below (at $\sigma_{cs}/\sigma_{ts} = +\infty$) and from above (at $\sigma_{cs}/\sigma_{ts} = 5$) according to

$$0.803 \approx \frac{\sqrt{13}}{2} - 1 \leq f \leq \frac{3\sqrt{13}}{5} - \frac{4}{5} \approx 1.363. \tag{23}$$

- In practice, the compressive strength σ_{cs} of the material being tested may be entirely unknown. In that case, the relatively tight inequalities (23) for the factor (22) can be used to obtain the lower and upper bounds

$$\sigma_{ts}^- := 0.803 \frac{P_{max}}{\pi RH} \leq \sigma_{ts} \leq 1.363 \frac{P_{max}}{\pi RH} =: \sigma_{ts}^+. \tag{24}$$

As a first step to gain insight into the accuracy of the formula (21), Table 2 reports its predictions for the three materials considered in Section 4 with compressive-to-tensile strength ratios $\sigma_{cs}/\sigma_{ts} = 5, 8,$ and 20 . For completeness, Table 2 also includes the corresponding values of the maximum force P_{max} , the factor (22), as well as of the lower and upper bounds (24). For all three materials, the formula (21) yields results for the uniaxial tensile strength σ_{ts} that are within 5% of the exact values.

To continue gaining insight into the accuracy of the formula (21), we are in the process of confronting it with experimental results for a variety of materials. We plan to report our findings in future parts of this work, where we will also highlight the critical importance of having experimental knowledge of large parts of the strength surface $\mathcal{F}(\sigma) = 0$ of the material, and not just of its uniaxial tensile strength σ_{ts} .

5.2. Comparisons with the ISRM and the ASTM formulas (1) and (2)

We close by circling back to the standardized formulas (1) and (2). Tables 3, 4, and 5 report their predictions for the three materials considered in Section 4 with compressive-to-tensile strength ratios $\sigma_{cs}/\sigma_{ts} = 5, 8,$ and 20 . When compared with the exact results — rather serendipitously, one may argue — the ISRM formula (1) for Brazilian tests carried out with curved ($R_p = 1.5R$) platens and the ASTM formula (1) for Brazilian tests carried out with flat ($R_p = +\infty$) platens perform reasonably well, more so for the specimens with the two largest compressive-to-tensile strength ratios $\sigma_{cs}/\sigma_{ts} = 8$ and 20 . The ASTM formula (2) for Brazilian tests carried out with curved ($R_p = 1.5R$) platens does not share the same fortune.

Table 3
Accuracy of the ISRM formula (1) for Brazilian tests carried out with curved ($R_p = 1.5R$) platens.

σ_{ts} (MPa)	σ_{cs}/σ_{ts}	P_{max} (kN)	Predicted σ_{ts} (MPa)	Error
200	5	125	159	26%
125	8	91	116	8%
50	20	4	55	9%

Table 4Accuracy of the ASTM formula (1) for Brazilian tests carried out with flat ($R_p = +\infty$) platens.

σ_{ts} (MPa)	$\sigma_{\text{cs}}/\sigma_{\text{ts}}$	P_{max} (kN)	Predicted σ_{ts} (MPa)	Error
200	5	116	148	35%
125	8	89	113	11%
50	20	41	53	6%

Table 5Accuracy of the ASTM formula (2) for Brazilian tests carried out with curved ($R_p = 1.5R$) platens.

σ_{ts} (MPa)	$\sigma_{\text{cs}}/\sigma_{\text{ts}}$	P_{max} (kN)	Predicted σ_{ts} (MPa)	Error
200	5	125	101	98%
125	8	91	74	37%
50	20	43	35	43%

CRedit authorship contribution statement

Aditya Kumar: Conceptualization, Methodology, Software, Writing – review & editing. **Yangyuanchen Liu:** Conceptualization, Methodology, Software, Writing – review & editing. **John E. Dolbow:** Conceptualization, Methodology, Supervision, Writing – review & editing, Funding acquisition. **Oscar Lopez-Pamies:** Conceptualization, Methodology, Supervision, Writing – original draft, Writing – review & editing, Funding acquisition.

Declaration of competing interest

The authors declare that they have no known competing financial interests or personal relationships that could have appeared to influence the work reported in this paper.

Data availability

Data will be made available on request.

Acknowledgments

This work was supported by the National Science Foundation, USA through the collaborative Grants CMMI–2132551 and CMMI–2132528. This support is gratefully acknowledged.

Appendix A. The derivation of the gap function (9)

By definition, the gap function in the boundary condition (8) is given by

$$\begin{aligned}
 g(\mathbf{u}(\mathbf{X}, t); \Delta d) &:= -\frac{(\mathbf{X} + \mathbf{u}(\mathbf{X}, t) - \mathbf{y}_p(\bar{\mathbf{X}}; \Delta d)) \cdot \mathbf{N}_p(\bar{\mathbf{X}})}{|\mathbf{X} + \mathbf{u}(\mathbf{X}, t) - \mathbf{y}_p(\bar{\mathbf{X}}; \Delta d)|} \|\mathbf{X} + \mathbf{u}(\mathbf{X}, t) - \mathbf{y}_p(\bar{\mathbf{X}}; \Delta d)\| \\
 &= -(\mathbf{X} + \mathbf{u}(\mathbf{X}, t) - \mathbf{y}_p(\bar{\mathbf{X}}; \Delta d)) \cdot \mathbf{N}_p(\bar{\mathbf{X}}),
 \end{aligned} \tag{25}$$

where

$$\mathbf{y}_p(\mathbf{Y}; \Delta d) = \begin{cases} \mathbf{Y} - \frac{\Delta d}{2} \mathbf{e}_2, & Y_2 > 0 \\ \mathbf{Y} + \frac{\Delta d}{2} \mathbf{e}_2, & Y_2 < 0 \end{cases} \quad \text{and} \quad \mathbf{N}_p(\mathbf{Y}) = \begin{cases} -\frac{1}{R_p} (Y_1 \mathbf{e}_1 + \sqrt{R_p^2 - Y_1^2} \mathbf{e}_2), & Y_2 > 0 \\ -\frac{1}{R_p} (Y_1 \mathbf{e}_1 - \sqrt{R_p^2 - Y_1^2} \mathbf{e}_2), & Y_2 < 0 \end{cases}$$

stand, respectively, for the deformation field (rigid translation) of the platens and for the outward unit normal of the surface

$$\Gamma_p = \Gamma_p^T \cup \Gamma_p^B \quad \text{with} \quad \begin{cases} \Gamma_p^T = \{\mathbf{Y} : \sqrt{Y_1^2 + (Y_2 - R + R_p)^2} = R_p, Y_2 > 0, |Y_3| < \frac{H_p}{2}\} \\ \Gamma_p^B = \{\mathbf{Y} : \sqrt{Y_1^2 + (Y_2 + R - R_p)^2} = R_p, Y_2 < 0, |Y_3| < \frac{H_p}{2}\} \end{cases} \tag{26}$$

of the platens that may come in contact with the specimen during the loading process, while

$$\bar{\mathbf{X}} = \arg \min_{\mathbf{Y} \in \Gamma_p} \|\mathbf{X} + \mathbf{u}(\mathbf{X}, t) - \mathbf{y}_p(\mathbf{Y}; \Delta d)\|$$

is the material point on the surface (26) of the platens whose image $y_p(\bar{\mathbf{X}}; \Delta d)$ is closest to the image $\mathbf{x} = \mathbf{X} + \mathbf{u}(\mathbf{X}, t)$ of the material point \mathbf{X} on the lateral boundary $\partial\Omega_L$ of the specimen at any given change in separation Δd between the platens.

A standard calculation shows that

$$\bar{\mathbf{X}} = \begin{cases} \frac{R_p x_1}{\sqrt{x_1^2 + \left(x_2 - R + R_p + \frac{\Delta d}{2}\right)^2}} \mathbf{e}_1 + \frac{R_p \sqrt{\left(x_2 - R + R_p + \frac{\Delta d}{2}\right)^2}}{\sqrt{x_1^2 + \left(x_2 - R + R_p + \frac{\Delta d}{2}\right)^2}} + R - R_p \mathbf{e}_2 + x_3 \mathbf{e}_3, & X_2 > 0 \\ \frac{R_p x_1}{\sqrt{x_1^2 + \left(x_2 + R - R_p - \frac{\Delta d}{2}\right)^2}} \mathbf{e}_1 - \frac{R_p \sqrt{\left(x_2 + R - R_p - \frac{\Delta d}{2}\right)^2}}{\sqrt{x_1^2 + \left(x_2 + R - R_p - \frac{\Delta d}{2}\right)^2}} + R - R_p \mathbf{e}_2 + x_3 \mathbf{e}_3, & X_2 < 0 \end{cases},$$

where we have made use of the indicial notation $x_i = X_i + u_i(\mathbf{X}, t)$. With the above results at hand, the gap function (25) can be written in the fully explicit form

$$g(\mathbf{u}(\mathbf{X}, t); \Delta d) = \begin{cases} \frac{1}{R_p} (x_1 - \bar{X}_1) \bar{X}_1 + \frac{1}{R_p} \left(x_2 - \bar{X}_2 + \frac{\Delta d}{2}\right) \sqrt{R_p^2 - \bar{X}_1^2}, & X_2 > 0 \\ \frac{1}{R_p} (x_1 - \bar{X}_1) \bar{X}_1 - \frac{1}{R_p} \left(x_2 - \bar{X}_2 - \frac{\Delta d}{2}\right) \sqrt{R_p^2 - \bar{X}_1^2}, & X_2 < 0 \end{cases}. \quad (27)$$

Now, the result (27) is general in that it applies to large changes in separation Δd between the platens. Leveraging the fact that the focus here is on specimens whose mechanical response can be described as linear elastic brittle, it is necessary to consider (27) in the limit of small deformations. To that end, define ζ as a vanishingly small parameter and consider that Δd and \mathbf{u} are of $O(\zeta)$. In the limit as $\zeta \searrow 0$, the gap function (27) reduces, to $O(\zeta)$, to the expression (9) in the main body of the text.

Appendix B. The augmented Lagrangian treatment of the contact boundary condition

Following, e.g., Simo and Laursen (1992), the augmented Lagrangian treatment of the contact boundary condition (11)₃ amounts to the replacement of the right-hand side of (11)₃ by

$$-\left\langle \Lambda^{(k)} + \frac{1}{\xi R E} g(\mathbf{u}^{(k)}; \Delta d) \right\rangle \mathbf{N},$$

where $\Lambda^{(k)} \geq 0$ is a fixed estimate of the Lagrange multiplier Λ that would make the constraint (8) be satisfied exactly. The superscript (k) in this last expression reflects the fact that the treatment involves an iteration process, one where the problem

$$\begin{cases} \operatorname{div} \left[\frac{1}{2(1+\nu)} (\nabla \mathbf{u}^{(k)} + \nabla \mathbf{u}^{(k)T}) + \frac{\nu}{(1+\nu)(1-2\nu)} (\operatorname{div} \mathbf{u}^{(k)}) \mathbf{I} \right] = \mathbf{0}, & (\mathbf{X}, t) \in \Omega \times [0, T] \\ \left[\frac{1}{2(1+\nu)} (\nabla \mathbf{u}^{(k)} + \nabla \mathbf{u}^{(k)T}) + \frac{\nu}{(1+\nu)(1-2\nu)} (\operatorname{div} \mathbf{u}^{(k)}) \mathbf{I} \right] \mathbf{N} = \mathbf{0}, & (\mathbf{X}, t) \in \partial\Omega_F \cup \partial\Omega_B \times [0, T] \\ \left[\frac{1}{2(1+\nu)} (\nabla \mathbf{u}^{(k)} + \nabla \mathbf{u}^{(k)T}) + \frac{\nu}{(1+\nu)(1-2\nu)} (\operatorname{div} \mathbf{u}^{(k)}) \mathbf{I} \right] \mathbf{N} = -\left\langle \Lambda^{(k)} + \frac{1}{\xi R E} g(\mathbf{u}^{(k)}; \Delta d) \right\rangle \mathbf{N}, & (\mathbf{X}, t) \in \partial\Omega_L \times [0, T] \\ \mathbf{u}^{(k)}(\mathbf{X}, 0) = \mathbf{0}, & \mathbf{X} \in \Omega \end{cases},$$

is solved for $\mathbf{u}^{(k)}$ followed by an update of the multiplier

$$\Lambda^{(k+1)} = \left\langle \Lambda^{(k)} + \frac{1}{\xi R E} g(\mathbf{u}^{(k)}; \Delta d) \right\rangle$$

until the tolerance $\max\{g(\mathbf{u}^{(k)}; \Delta d)\} \leq \operatorname{To1}_g$ is reached. For all the calculations presented in the main body of the text, $\Lambda^{(0)} = 0$, $\operatorname{To1}_g = 10^{-6} R$, and $\xi^{-1} = 10^{-2} E$.

Appendix C. A comment on the intrinsic material length scales in the fracture theory (14)–(15)

As noted in Remark 8 in the main body of the text, a key aspect of the fracture theory (14)–(15) is that it features (not just one but) a family of intrinsic material length scales.

To illustrate this key aspect, Fig. 12 presents the predictions from the theory for the critical values σ_c of the applied stress σ at which fracture nucleates from the pre-existing crack in single-edge crack specimens subjected to uniaxial tension and in slanted center crack specimens subjected to equibiaxial tension; see the insets in Figs. 12(a) and 12(b). The results pertain to thin rectangular plates, of height $L = 600$ mm and width $B = 200$ mm for the specimens under uniaxial tension and of height $L = 600$ mm and width $B = L = 600$ mm for the specimens under equibiaxial tension, that are made of a material with Young's modulus $E = 100$ GPa, Poisson's ratio $\nu = 0.20$, Drucker–Prager strength surface with tensile and compressive strength $\sigma_{tS} = 200$ MPa and $\sigma_{cS} = 1000$ MPa, and critical energy release rate $G_c = 1000$ N/m. For both problems, it suffices to consider the same value of regularization length

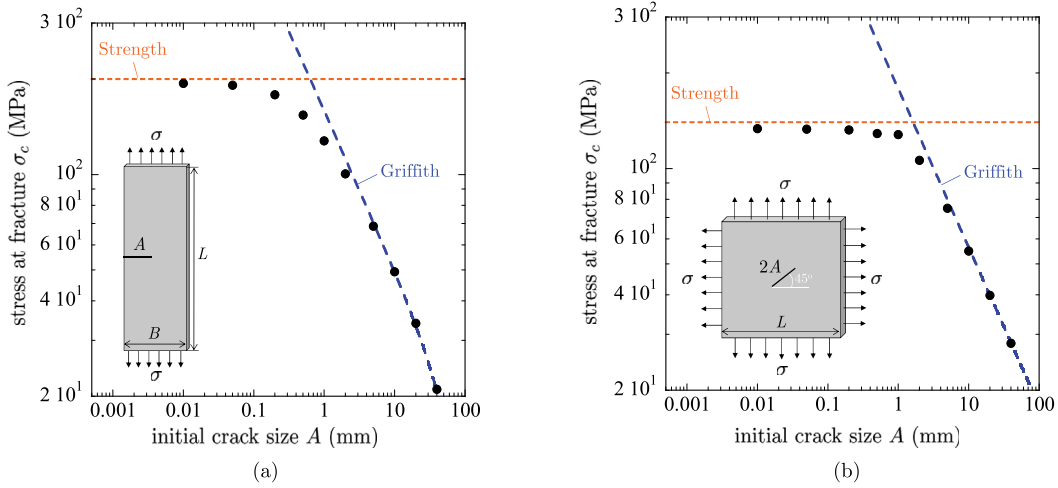


Fig. 12. Theoretical predictions — from the simulations of the tests schematically depicted in the insets — illustrating the transition from Griffith-dominated to strength-dominated nucleation of fracture as the size A of the crack decreases from large to small. The results show the critical stress σ_c at which fracture nucleates from the crack as a function of its size A . For direct comparison, the plots include the predictions of nucleation based on the Griffith competition between the elastic and fracture energies (blue dashed line) and based on strength (orange dotted line). The intercepts between these two limiting results — $A = 0.63$ mm in part (a) and $A = 1.56$ mm in part (b) — roughly identify the material length scales built in the theory corresponding to these two cases.

as in Section 4, namely, $\varepsilon = 0.5$ mm. The corresponding value for the parameter δ^f is 2.65; see Table 1. The results are shown as a function of the size A of the pre-existing crack. For the slanted center crack specimens, the crack is oriented at $\theta = 45^\circ$ with respect to the axis of symmetry of the specimen.

Given that both configurations are classical problems in linear elastic fracture mechanics, there are well established formulas for the critical values σ_c at which *large cracks* start growing. They read (Tada et al., 1973)

$$\sigma_c = \frac{\cos\left(\frac{\pi A}{2B}\right) \sqrt{\frac{G_c E}{\pi A}}}{\left[0.752 + 2.02 \frac{A}{B} + 0.37 \left(1 - \sin\left(\frac{\pi A}{2B}\right)\right)^3\right] \sqrt{\frac{2B}{\pi A} \tan\left(\frac{\pi A}{2B}\right)}} \quad (28)$$

for the single-edge crack specimens under uniaxial tension and (Sih et al., 1962)

$$\sigma_c = \sqrt{\frac{G_c E}{\pi A}} \quad (29)$$

for the slanted center crack specimens under equibiaxial tension. In the opposite limit of *small cracks*, it is trivial to deduce that

$$\sigma_c = \sigma_{ts} \quad (30)$$

for the specimens under uniaxial tension and

$$\sigma_c = \frac{2\sigma_{cs}\sigma_{ts}}{3\sigma_{cs} - \sigma_{ts}} \equiv \sigma_{bs} \quad (31)$$

for the specimens under equibiaxial tension, where we have introduced the notation σ_{bs} to denote the biaxial tensile strength of the material. Both sets of limiting results (28)–(29) and (30)–(31) are plotted in Fig. 12 to aid the discussion.

The results in Fig. 12(a) show that for crack sizes $A > 2$ mm, nucleation of fracture is characterized by the Griffith competition between the elastic and fracture energies of the material (blue dashed line). On the other hand, for crack sizes $A < 0.02$ mm, nucleation of fracture is characterized by the strength of the material (orange dotted line), in this case, its uniaxial tensile strength $\sigma_{ts} = 200$ MPa. Finally, for crack sizes in the intermediate range $A \in [0.02, 2]$ mm, the results show that nucleation of fracture is characterized by an interpolation between the strength and the Griffith competition between the elastic and fracture energies. The material length scale in this case is thus about 0.2 mm.

Similar to Fig. 12(a), the results in Fig. 12(b) show that for crack sizes $A > 5$ mm, nucleation of fracture is characterized by the Griffith competition between the elastic and fracture energies of the material (blue dashed line), while for crack sizes $A < 0.05$ mm, nucleation of fracture is characterized by the strength of the material (orange dotted line), in this case, its biaxial tensile strength $\sigma_{bs} = 143$ MPa. For crack sizes in the intermediate range $A \in [0.05, 5]$ mm, the results show that nucleation of fracture is characterized by an interpolation between the strength and the Griffith competition between the elastic and fracture energies. The material length scale in this case is thus about 0.5 mm.

Appendix D. The classical solution of Hondros (1959)

One of the classical contributions in the study of the Brazilian test is that of Hondros (1959) who worked out the stress field in the specimen under the idealizations that the platens apply a uniform pressure p over an arc length a , so that $p = P/(Ha)$, and that the state of stress is plane stress. By now, it has been well established that, irrespective of their radius of curvature, the platens do *not* apply a uniform pressure to the specimen, but one that is strongly non-uniform. It has also been well established that, prior to fracture, the stress fields that result in the specimen are essentially insensitive to the specifics of the non-uniform pressure distribution applied by the platens, save, obviously, at the contact and the region immediately below; see, e.g., (Kourkoulis et al., 2013; Yuan and Shen, 2017). This insensitivity justifies the use of the classical solution of Hondros (1959) away from the platens.

According to the solution of Hondros (1959), the principal stresses along the loading axis of symmetry in a specimen of radius R and thickness H are given by

$$\left\{ \begin{array}{l} \sigma_1(0, X_2, 0) = \frac{\frac{2P}{\pi Ha} \left(1 - \frac{X_2^2}{R^2}\right) \sin\left(\frac{a}{R}\right)}{1 - 2\frac{X_2^2}{R^2} \cos\left(\frac{a}{R}\right) + \frac{X_2^4}{R^4}} - \frac{2P}{\pi Ha} \arctan \left[\frac{1 + \frac{X_2^2}{R^2} \tan\left(\frac{a}{2R}\right)}{1 - \frac{X_2^2}{R^2}} \right] \\ \sigma_2(0, X_2, 0) = -\frac{\frac{2P}{\pi Ha} \left(1 - \frac{X_2^2}{R^2}\right) \sin\left(\frac{a}{R}\right)}{1 - 2\frac{X_2^2}{R^2} \cos\left(\frac{a}{R}\right) + \frac{X_2^4}{R^4}} - \frac{2P}{\pi Ha} \arctan \left[\frac{1 + \frac{X_2^2}{R^2} \tan\left(\frac{a}{2R}\right)}{1 - \frac{X_2^2}{R^2}} \right] \\ \sigma_3(0, X_2, 0) = 0 \end{array} \right. ,$$

where, again, P is the total force applied by the platens, a is the arc length over which the uniform pressure $p = P/(Ha)$ is applied, and where we recall that the origin of the laboratory frame of reference is placed at the center of the specimen; see Fig. 1. Two remarks are in order from these expressions. First, note that $\sigma_2 \leq 0$ for all $|X_2| \leq R$. Second, for small a relative to R ,

$$\sigma_1(0, 0, 0) = \frac{P}{\pi RH}, \quad \sigma_2(0, 0, 0) = -\frac{3P}{\pi RH}.$$

That is, irrespective of the applied force P , $\sigma_1 \geq 0$ and $\sigma_1/\sigma_2 = -1/3$ at the center of the specimen. This is the result used to establish the relation (20) in the main body of the text.

References

- Andreev, G.E., 1991. A review of the Brazilian test for rock tensile strength determination. Part I: calculation formula. *Mini. Sci. Technol.* 13, 445–456.
- ASTM, 2008. D 3967-08. Standard Test Method for Splitting Tensile Strength of Intact Rock Core Specimens. ASTM International, West Conshohocken, USA.
- ASTM, 2016. D 3967-16. Standard Test Method for Splitting Tensile Strength of Intact Rock Core Specimens. ASTM International, West Conshohocken, USA.
- Awaji, H., Sato, S., 1979. Diametral compressive testing method. *J. Eng. Mater. Technol.* 101, 139–147.
- Bourdin, B., Francfort, G.A., Marigo, J.J., 2000. Numerical experiments in revisited brittle fracture. *J. Mech. Phys. Solids* 48, 797–826.
- Carneiro, F.L.L.B., 1943. A new method to determine the tensile strength of concrete. In: *Proceedings of the 5th Meeting of the Brazilian Association for Technical Rules*. pp. 126–129.
- Colback, P.S.B., 1966. An analysis of brittle fracture initiation and propagation in the Brazilian test. In: *Proceedings of the First Congress of the International Society of Rock Mechanics*. Lisbon, Portugal, pp. 385–391.
- Drucker, D.C., Prager, W., 1952. Soil mechanics and plastic analysis for limit design. *Quart. Appl. Math.* 10, 157–165.
- Ely, R.E., 1972. Strength of titania and aluminum silicate under combined stresses. *J. Am. Ceram. Soc.* 55, 347–350.
- Eraslan, N., Williams, D.J., 2012. Experimental, numerical and analytical studies on tensile strength of rocks. *Int. J. Rock Mech. Min. Sci.* 49, 21–30.
- Fairbairn, E., Ulm, F., 2002. A tribute to Fernando L.L.B. Carneiro (1913–2001) engineer and scientist who invented the Brazilian test. *Mater. Struct.* 35, 195–196.
- Fairhurst, C., 1964. On the validity of the ‘Brazilian’ test for brittle materials. *Int. J. Rock Mech. Min. Sci. Geomech.* 1, 535–546.
- Francfort, G.A., Giacomini, A., Lopez-Pamies, O., 2019. Fracture with healing: A first step towards a new view of cavitation. *Anal. PDE* 12, 417–447.
- Francfort, G.A., Marigo, J.J., 1998. Revisiting brittle fracture as an energy minimization problem. *J. Mech. Phys. Solids* 46, 1319–1342.
- Garcia, V.J., Marquez, C.O., Zuñiga-Suarez, A.R., Zuñiga-Torres, B.C., Villalta-Granda, L.J., 2017. Brazilian test of concrete specimens subjected to different loading geometries: review and new insights. *Int. J. Concr. Struct. Mater.* 11, 343–363.
- Garcia-Fernandez, C.C., Gonzalez-Nicieza, C., Alvarez-Fernandez, M.I., Gutierrez-Moizant, R.A., 2018. Analytical and experimental study of failure onset during a Brazilian test. *Int. J. Rock Mech. Min. Sci.* 103, 254–265.
- Griffith, A.A., 1921. The phenomena of rupture and flow in solids. *Philos. Trans. R. Soc. Lond. Ser. A* 221, 163–198.
- Hondros, G., 1959. The evaluation of Poisson’s ratio and the modulus of materials of a low tensile resistance by the Brazilian (indirect tensile) test with particular reference to concrete. *Aust. J. Appl. Sci.* 10, 243–268.
- ISRM, 1978. International society for rock mechanics. Suggested methods for determining tensile strength of rock materials. *Int. J. Rock Mech. Min. Sci. Geomech.* 15, 99–103.
- Kikuchi, N., Oden, J.T., 1988. *Contact Problems in Elasticity: A Study of Variational Inequalities and Finite Element Methods*. SIAM, Philadelphia.
- Kourkoulis, S.K., Markides, C.F., Chatzistergos, P.E., 2013. The standardized Brazilian disc test as a contact problem. *Int. J. Rock Mech. Min. Sci.* 57, 132–141.
- Kumar, A., Bourdin, B., Francfort, G.A., Lopez-Pamies, O., 2020. Revisiting nucleation in the phase-field approach to brittle fracture. *J. Mech. Phys. Solids* 142, 104027.
- Kumar, A., Francfort, G.A., Lopez-Pamies, O., 2018a. Fracture and healing of elastomers: A phase-transition theory and numerical implementation. *J. Mech. Phys. Solids* 112, 523–551.
- Kumar, A., Lopez-Pamies, O., 2020. The phase-field approach to self-healable fracture of elastomers: A model accounting for fracture nucleation at large, with application to a class of conspicuous experiments. *Theor. Appl. Fract. Mech.* 107, 102550.
- Kumar, A., Lopez-Pamies, O., 2021. The poker-chip experiments of gent and lindley (1959) explained. *J. Mech. Phys. Solids* 150, 104359.

- Kumar, A., Ravi-Chandar, K., Lopez-Pamies, O., 2018b. The configurational-forces view of fracture and healing in elastomers as a phase transition. *Int. J. Fract.* 213, 1–16.
- Kumar, A., Ravi-Chandar, K., Lopez-Pamies, O., 2022. The revisited phase-field approach to brittle fracture: Application to indentation and notch problems. *Int. J. Fract.* 237, 83–100.
- Laursen, T.A., 2003. *Computational Contact and Impact Mechanics*. Springer-Verlag, Berlin.
- Li, D., Wong, L.N.Y., 2013. The Brazilian disc test for rock mechanics applications: Review and new insights. *Rock Mech. Rock Eng.* 46, 269–287.
- Lopez-Pamies, O., 2023. Strength revisited: One of three basic ingredients needed for a complete macroscopic theory of fracture. <https://imechanica.org/node/26641>.
- Oden, J.T., Kikuchi, N., Song, Y.J., 1980. *Reduced Integration and Exterior Penalty Methods for Finite Element Approximations of Contact Problems in Incompressible Elasticity*. TICOM Report 80-2, The University of Texas at Austin.
- Poulain, X., Lefèvre, V., Lopez-Pamies, O., Ravi-Chandar, K., 2017. Damage in elastomers: Nucleation and growth of cavities, micro-cracks, and macro-cracks. *Int. J. Fract.* 205, 1–21.
- Poulain, X., Lopez-Pamies, O., Ravi-Chandar, K., 2018. Damage in elastomers: Healing of internally nucleated cavities and micro-cracks. *Soft Matter* 14, 4633–4640.
- Sih, G.C., Paris, P.C., Erdogan, F., 1962. Crack-tip, stress-intensity factors for plane extension and plate bending problems. *J. Appl. Mech.* 29, 306–312.
- Simo, J.C., Laursen, T.A., 1992. An augmented Lagrangian treatment of contact problems involving friction. *Comput. Struct.* 42, 97–116.
- Tada, H., Paris, P.C., Irwin, G.R., 1973. *The Stress Analysis of Cracks Handbook 3rd Edition*. The American Society of Mechanical Engineers, New York.
- Wong, L.N.Y., Zou, C., Cheng, Y., 2014. Fracturing and failure behavior of carrara marble in quasistatic and dynamic Brazilian disc tests. *Rock Mech. Rock Eng.* 47, 1117–1133.
- Wriggers, P., 2006. *Computational Contact Mechanics*. Springer-Verlag, Berlin.
- Yuan, R., Shen, B., 2017. Numerical modelling of the contact condition of a Brazilian disk test and its influence on the tensile strength of rock. *Int. J. Rock Mech. Min. Sci.* 93, 54–65.